A local subset of mesenchymal cells expressing the transcription factor Osr1 orchestrates lymph node initiation

Pedro Vallecillo-García, Mickael Orgeur, Glenda Comai, Sophie Poehle-Kronawitter, Cornelius Fischer, Marleen Gloger, Camille Dumas, Claudia Giesecke-Thiel, Sascha Sauer, Shahragim Tajbakhsh, et al.

▶ **To cite this version:**

Pedro Vallecillo-García, Mickael Orgeur, Glenda Comai, Sophie Poehle-Kronawitter, Cornelius Fischer, et al.. A local subset of mesenchymal cells expressing the transcription factor Osr1 orchestrates lymph node initiation. Immunity, 2023, 56 (6), pp.1204-1219.e8. 10.1016/j.immuni.2023.04.014 . hal-04257866

HAL Id: hal-04257866
https://hal.science/hal-04257866

Submitted on 25 Oct 2023

HAL is a multi-disciplinary open access archive for the deposit and dissemination of scientific research documents, whether they are published or not. The documents may come from teaching and research institutions in France or abroad, or from public or private research centers.

L'archive ouverte pluridisciplinaire **HAL**, est destinée au dépôt et à la diffusion de documents scientifiques de niveau recherche, publiés ou non, émanant des établissements d'enseignement et de recherche français ou étrangers, des laboratoires publics ou privés.

Distributed under a Creative Commons Attribution - NonCommercial - NoDerivatives 4.0 International License

1

“Mesenchymal Osr1 cells orchestrate lymph node initiation”

Pedro Vallecillo-García[1,10,*], Mickael Orgeur[2], Glenda Comai[3], Sophie Poehle-Kronnawitter[1], Cornelius Fischer[4], Marleen Gloger[5,6], Camille Dumas[7], Claudia Giesecke-Thiel[8], Sascha Sauer[4], Robert Kelly[7], Shahragim Tajbakhsh[3], Uta E. Höpken[9] and Sigmar Stricker[1,*]

[1] Institute for Chemistry and Biochemistry, Freie Universität Berlin, 14195, Berlin, Germany

[2] Institut Pasteur, Université Paris Cité, CNRS UMR 6047, Unit for Integrated Mycobacterial Pathogenomics, 75015 Paris, France

[3] Institut Pasteur, Stem Cells & Development Unit, CNRS UMR 3738, Paris, France

[4] Core Facility Genomics, Berlin Institute of Health at Charité, 10178, Berlin, Germany; Max Delbrück Center for Molecular Medicine in the Helmholtz Association, 10115, Berlin, Germany

[5] Max Delbrück Center for Molecular Medicine, Department of Translational Tumor Immunology, 13125, Berlin, Germany

[6] Uppsala University, Immunology Genetics and Pathology, 75237, Uppsala, Sweden

[7] Aix-Marseille Université, CNRS UMR 7288, IBDM, 13009, Marseille, France

[8] Max Planck Institute for Molecular Genetics, 14195, Berlin, Germany

[9] Max Delbrück Center for Molecular Medicine, Department of Microenvironmental Regulation in Autoimmunity and Cancer, 13125, Berlin, Germany

[10] Lead Contact

*Correspondence: sigmar.stricker@fu-berlin.de, vallecillo@zedat.fu-berlin.de

Abstract

The emergence of lymph nodes (LNs) is orchestrated by lymphoid tissue organizer cells (LTos) that attract and retain lymphoid tissue inducer cells (LTis) at strategic positions in the embryo. Identity and mode of action applied by LTos during the first LTi attraction have remained poorly characterized. Here, we show that cells expressing the gene *Osr1* are mesenchymal LTo progenitors. By dissecting Osr1+ cell heterogeneity we demonstrate distinct mesenchymal LTo signatures at diverse anatomical locations and reveal a common progenitor of mesenchymal LTos and LN-associated adipose tissue. *Osr1* is essential for LN initiation, driving commitment of mesenchymal LTos independently of neural retinoic acid, and for LN-associated lymphatic vasculature. Finally, we demonstrate that combined action of CXCL13 and CCL21 is required for LN initiation. Our results substantially redefine the role and identity of mesenchymal organizer cells and unify current views proposing a new model of cooperative cell function in LN initiation.

Introduction

Secondary lymphoid organs (SLOs) provide infrastructure for efficient immune response and comprise lymph nodes (LNs), Peyer's patches (PPs), mucosa-associated lymphoid tissue (MALT) and the spleen. LNs emerge during development at strategic vascular junctions in the embryo. LN organogenesis is initiated by the accumulation of so-called lymphoid tissue inducer cells (LTis) at the prospective sites of LN formation as the first step in a cascade of events leading to mature LN formation. LTis belong to the family of innate lymphoid cells (ILCs) (1-3), which originate from the hemogenic endothelium and colonize the fetal liver (4).

LTis accumulate at specific sites of the embryo relying on the positional information provided by lymphoid tissue organizer cells (LTos) (1, 5-7). The exact identity of LTos and their developmental origin remain obscure. Of note, despite their similar functions, mesenchymal LTos in LNs and spleen have different developmental origins (8-10). LNs are embedded in white adipose tissue (WAT), and adipogenic progenitor cells (APCs) can be reprogrammed as mesenchymal stromal cells in LNs via LTRβ signaling (11). This indicates a common origin of both cell types during development.

Acquisition of CXCL13 expression was described as the first step in mesenchymal LTo commitment (6). *Cxcl13* expression in the embryo is highly restricted to the region of LN appearance and its activation has been linked to the secretion of retinoic acid (RA) by motoneurons adjacent to the LN anlage (12). RA signaling is considered crucial for LN formation, as mice lacking the RA receptor-related orphan receptor gamma (RORγt) are devoid of LNs (1, 13), and LTi differentiation in LN anlagen depends on RA signaling (14).

Subsequently, lymphotoxin-αβ (Ltαβ) expressed by LTi cells signals to LTos expressing the lymphotoxin receptor beta (LTβR) (5, 6), driving LNs organogenesis. This leads to a positive feedback loop that results in increased secretion of chemokines including CXCL13 and CCL21 reinforcing LTi recruitment and retention, and the expression of cell adhesion molecules required for LTo differentiation (1, 5, 6). The initial secretion of CXCL13 and CCL21, however, appears independent of LTβR signaling (12, 15).

CXCL13 is seen as a crucial factor in LN initiation, as mouse models lacking either *Cxcl13* or its receptor *Cxcr5* resulted in LN initiation arrest in the majority of peripheral LNs although cervical and mesenteric LNs were formed (12, 16-18). Depletion of lymphatic endothelial cells (LECs) does not impair LN initiation, however LECs are important for LN formation (19). Indeed, recent studies ascribed LTo functions to lymphatic and blood endothelial cells (20, 21). This suggests that, in addition to LTi recruitment via the CXCL13/CXCR5 axis, additional factors emanating from LTos (mesenchymal and endothelial) may be involved to achieve effective first retention of LTis in the LN anlage. Importantly, LNs develop at different body locations; although similar strategies might be shared this may implicate the interaction of diverse local cell types and signaling molecules. Therefore, deciphering the initial steps of LN formation and assessing local tissue heterogeneities might reveal similar strategies in the organogenesis of more adaptive lymphoid organs such as MALT or tertiary lymphoid organs (TLOs).

Here, we identify a subset of Odd-skipped related transcription factor 1-positive (Osr1+) cells in the embryo as a common progenitor of mesenchymal LTos and APCs. *Osr1* is required for both, mesenchymal LTo commitment and assembly of LN-associated lymphatic vasculature. Our results challenge the current model of neuron-derived RA in LN initiation and redefine the initial steps of LN formation, where combined chemokine-directed LTi attraction by mesenchymal and lymphatic endothelial LTos results in LN initiation.

Results

Osr1 marks mesenchymal LTo progenitors and progenitors of all adult LN mesenchymal stromal subpopulations

The identity of embryonic mesenchymal precursors involved in LN formation has been hampered by the lack of specific markers. We have previously shown that WAT and skeletal muscle connective tissue (MCT) stromal cells share a common origin during development in a subpopulation of lateral plate mesoderm-derived cells expressing the transcription factor Osr1 (22). *Osr1* plays a key role in the formation of embryonic organs such as kidney, heart, foregut and skeletal muscle (22-25), however a function in LNs has not been described. *Osr1* expression, visualized via an eGFP knock-in reporter (*Osr1*^{GCE}), was detected prior to LTi accumulation at stage E12.5 in the axillary area. Osr1+ cells were found in the mesenchyme that surrounds the bifurcation of the lateral thoracic vein and include the first CXCL13+ cells (Figure 1A). At E14.5, when the LN anlage organizes with the attraction of the first LTi cells, Osr1+ cells localized in the cervical and axillary regions in direct contact with CD4+ LTi cells and in association with the developing lymphatic vasculature (Figure 1A and S1A). At this stage, Osr1+ cells were only observed adjacent to the outer endothelial cell layer in the thymus and were absent in the spleen (Figure S1B). Later, *Osr1* expression faded in the LN anlagen. At E16.5, Osr1+ cells were found sparsely in close association with CD4+ cells and at E19.5 only few Osr1+ cells were found in the LN anlage (Figure 1B). In adult peripheral and mesenteric LNs, *Osr1* expression visualized via a beta galactosidase knock-in reporter (*Osr1*^{LacZ}) was restricted to the medullary region of LNs and PPs (Figure 1C), consistent with the *Osr1* expression found in Nr4a1+, Inmt+ and CD34+ stromal subpopulations (26).

Embryonic pulse-labeling of Osr1+ cells via tamoxifen administration at E11.5 and E12.5 in *Rosa26*$^{mTmG/+}$ *Osr1*$^{GCE/+}$ animals revealed that Osr1 descendants were broadly distributed between the medulla and the capsule in adult LNs (Figure 1D). Osr1 descendants were found inside the B cell follicle co-expressing CXCL13 or CD21/CD35, specific markers for follicular dendritic cells (FDCs) (Figure 1E), in the cortex expressing ERTR7 or PDPN marking T cell zone fibroblastic reticular cells (TRCs) (Figure 1F), and in the subcapsular sinus expressing MAdCAM-1 marking marginal reticular cells (MRCs) (Figure 1G). Thus, FDCs, TRCs, and MRCs can originate from a common embryonic progenitor already present at stage E11.5/12.5. In addition, we found Osr1 descendants giving rise to pericytes in close association with PNAd+ high endothelial venules (HEV), and to pericytes expressing PDGFRβ associated with blood endothelial cells and adjacent to LYVE1+ lymphatic vasculature (Figure S1C). Contrary to LNs, the splenic stroma was devoid of embryonic-derived Osr1+ cells (Figure S1C). In line with the decreasing expression of *Osr1* in fetal LNs, membrane GFP+ traced cells were rarely found in the adult LN stroma after a pulse of tamoxifen at postnatal days 0 and 1 (Figure S1D) or in E18.5 axillary LN stroma after a tamoxifen pulse at E15.5 (Figure S1E). Next, we measured mGFP contribution to stromal subpopulations via flow cytometry analysis of peripheral LNs (PLNs) (Figure 1H). Labelling by E11.5/12.5 tamoxifen pulsing, we found that approximately a quarter of the PDPN+ CD31- FRCs were Osr1 descendants (Figure 1I). Contribution to the double negative population (PDPN- CD31-) was low and contribution to LECs (PDPN+ CD31+) and BECs (PDPN- CD31+) was practically not detected (Figure 1H). Quantification of embryonic lineage contribution to TRCs, FDCs and MRCs using FACS (Figure 1I) and section immunofluorescence (Figure 1J) highlighted a partial contribution to all populations. In line with the partial contribution in LNs, we observed partial embryonic Osr1+ contribution to stromal vascular fraction (SVF) in inguinal fat adipose tissue (Figure 1K).

In summary, *Osr1* marks a poorly described population of mesenchymal cells in the embryo at sites of prospective LN formation and prior to mesenchymal LTo commitment or LTi attraction. Thus, *Osr1* labels the first documented mesenchymal LTo progenitors, which also comprise an origin of adult mesenchymal subpopulations in the LN stroma.

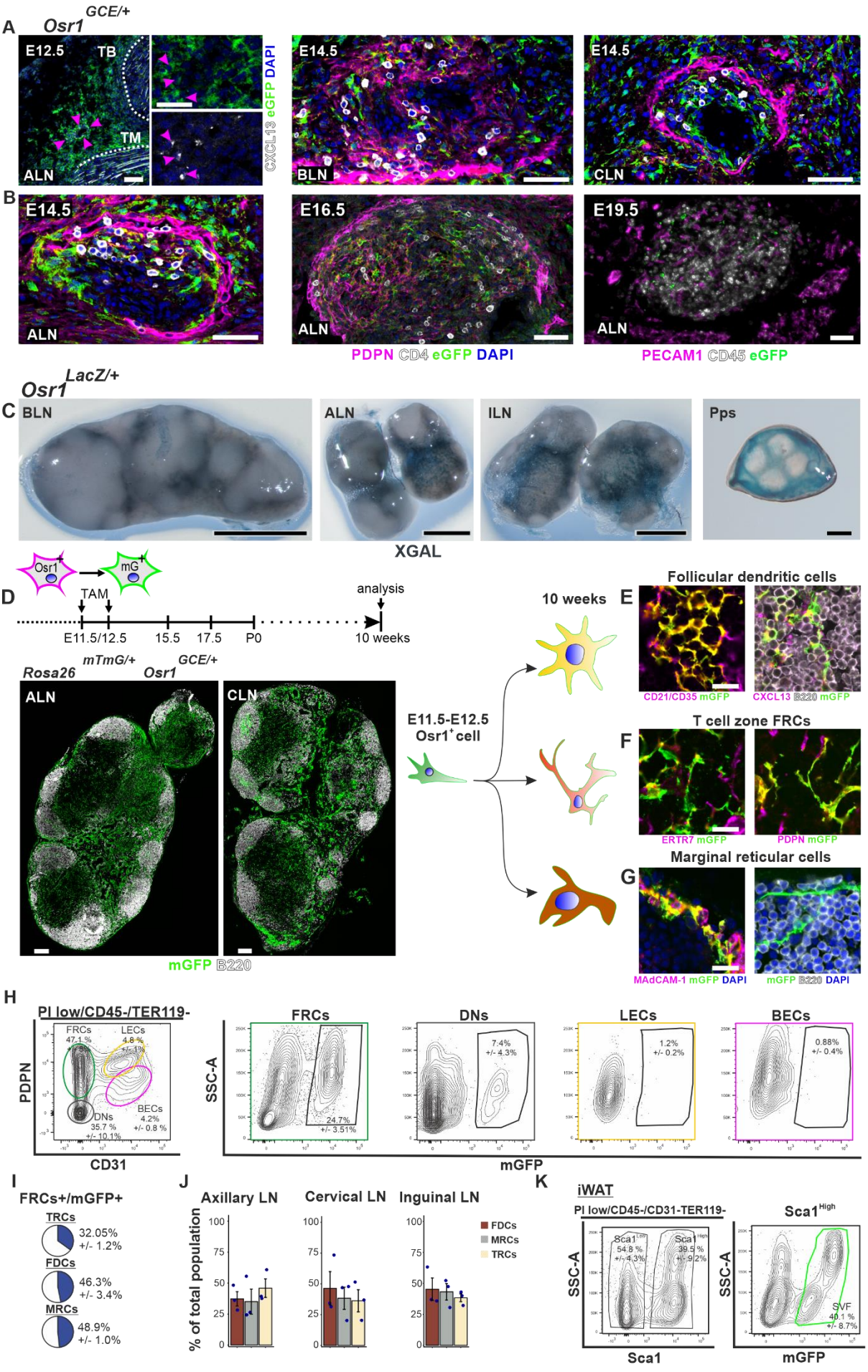
A
Osr1 GCE/+
E12.5
TB
TM
ALN
CXCL13 eGFP DAPI
E14.5
BLN
E14.5
CLN
B
E14.5
ALN
E16.5
ALN
PDPN CD4 eGFP DAPI
E19.5
ALN
PECAM1 CD45 eGFP
Osr1 LacZ/+
C
BLN
ALN
ILN
Pps
XGAL
D
Osr1+
mG+
TAM
E11.5/12.5
15.5
17.5
P0
analysis
10 weeks
Rosa26 mTmG/+ Osr1 GCE/+
ALN
CLN
mGFP B220
E11.5-E12.5 Osr1+ cell
10 weeks
E
Follicular dendritic cells
CD21/CD35 mGFP
CXCL13 B220 mGFP
F
T cell zone FRCs
ERTR7 mGFP
PDPN mGFP
G
Marginal reticular cells
MAdCAM-1 mGFP DAPI
mGFP B220 DAPI
H
PI low/CD45-/TER119-
FRCs 47.1 %
LECs 4.8 % +/- 1%
DNs 35.7 % +/- 10.1%
BECs 4.2% +/- 0.8 %
PDPN
CD31
FRCs
24.7% +/- 3.51%
DNs
7.4% +/- 4.3%
LECs
1.2% +/- 0.2%
BECs
0.88% +/- 0.4%
SSC-A
mGFP
I
FRCs+/mGFP+
TRCs
32.05% +/- 1.2%
FDCs
46.3% +/- 3.4%
MRCs
48.9% +/- 1.0%
J
Axillary LN
Cervical LN
Inguinal LN
FDCs
MRCs
TRCs
% of total population
K
iWAT
PI low/CD45-/CD31-TER119-
Sca1 54.8 % +/- 4.3%
Sca1 39.5 % +/- 9.2%
SSC-A
Sca1
Sca1High
SVF 40.1 % +/- 8.7%
mGFP

Figure 1. *Osr1 marks mesenchymal LTo progenitors, which are a source of adult mesenchymal stromal subpopulations.* ***(A, B)*** *Representative images of E12.5, E14.5, E16.5 and E19.5 Osr1$^{GCE/+}$ LNs. At E12.5, the axillary region contains the first Osr1+ cells (eGFP) expressing CXCL13 close to the lateral thoracic artery. Arrowheads point to sites of Osr1 and CXCL13 co-expression and boxed region is shown as a magnification at the right. At the stages E14.5, E16.5 and E19.5, immunofluorescence for PDPN, CD4/CD45 and eGFP (Osr1) shows Osr1 expression in cells intermingled with LTi cells and associated with the PDPN-high lymphatic vasculature. Dashed lines in* ***(A)*** *border teres major (TM) and triceps brachii (TB) muscles.* ***(C)*** *Osr1 expression in LNs and Pps from adult Osr1^{LacZ} reporter animals assessed by whole-tissue X-gal staining.* ***(D)*** *Schematic representation of tamoxifen injection for genetic lineage tracing. Lineage contribution was assessed at 10 weeks of age. Below: immunofluorescence of 10-week-old ALN and CLN sections for mGFP (Osr1 lineage) and B220 demarcating B cell follicle.* ***(E-G)*** *Representative immunofluorescence images of 10-week-old PLNs co-stained for mGFP and FDC markers CD21/CD35 and CXCL13, FRC markers ERTR7 and PDPN, and MRC marker MAdCAM-1.* ***(H)*** *Flow cytometry analysis from Rosa26$^{mTmG/+}$ Osr1$^{GCE/+}$ adult PLNs for Osr1 lineage (mGFP) contribution to FRCs, double negative cells (DNs), LECs and BECs.* ***(I)*** *Quantification of FRCs-mGFP+ FACS isolated cells expressing the markers PDPN, MADCAM1 and CD25/35.* ***(J)*** *Quantification of Osr1 embryonic lineage contribution to adult MRCs, FDCs and TRCs quantified on sections by immunolabeling for PDPN, MADCAM1 and CD25/35.* ***(K)*** *Flow cytometry analysis from Rosa26$^{mTmG/+}$ Osr1$^{GCE/+}$ adult inguinal fat pad to assess Osr1 lineage contribution to Sca1^{high} stromal vascular fraction. Representative images have been captured from at least 3 different embryos. Values are shown as percentage of the mean and as a +/- percentage of the s.e.m. In* ***H-K****, n=3. Scale bar represents in* ***(A)*** *50 µm,* ***(B)*** *1 mm,* ***(C)*** *200 µm and* ***(E-G)*** *10 µm. Abbreviations: ALN, axillary LN; BLN, brachial LN; CLN, cervical LN; ILN, inguinal LN; and Pps, Peyer´s patches.*

Dissecting embryonic Osr1+ cell heterogeneity at the single-cell level

At E13.5, CXCL13 expressing LTos were only found at the location of LN formation and represented a subpopulation of mesenchymal Osr1+ cells in the areas of peripheral and mesenteric LN anlagen (Figure 2A and S2A). At the transcriptional level, the vast majority of *Cxcl13* expression was found in Osr1+ cells (Figure S2B), confirming Osr1+ cells as a broader population that contains mesenchymal LTos. In order to dissect the heterogeneity of the Osr1+ cells and to characterize early mesenchymal LTos, we performed droplet-based single-cell RNA sequencing (scRNA-seq) of E13.5 *Osr1$^{GCE/+}$* cells isolated by FACS (Figure 2B). To enrich for Osr1+ cells associated with LN primordia, E13.5 *Osr1$^{GCE/+}$* embryos were dissected from the axilla until the tongue including the inguinal region. Following exclusion of low-quality cells and empty droplets (Figure S2C and Methods), 6,849 E13.5 Osr1+ cells were further analyzed by unsupervised clustering. The 15 clusters identified were visualized by fast interpolation-based *t*-distributed stochastic neighbor embedding (Flt-SNE) on two dimensions (Figure 2C). Based on the enrichment of key genes obtained after differential expression analysis (Figure S2D) and section immunofluorescence, we defined the Osr1+ cell subpopulations and assigned their presumptive anatomical locations (Figure 2D).

Given the restricted expression of the gene *Barx1* in the lower jaw and proximal limb region (27), we assigned clusters 5, 10, 12 and 13 to Osr1+ cells of the craniofacial region (Figure 2E and S2E). Complementary, clusters 1-4 and 6-9 contain Osr1+ cells anatomically located in the trunk. Cluster 5 contained salivary gland mesenchymal cells and MCT of the masseter muscle enriched in *Sfrp2* expression (Figure 2E-G). Cluster 10 expressed *Pax3* suggesting mesenchymal cells of the frontal low mandible mesenchyme (28). Cluster 12 showed expression of *Pax9* and *Dach1*, which converge only at the dorsal mesenchyme of the lower jaw flanking the tongue (29), both regions rich in Osr1+ cells (Figure 2E-G). Cluster 13 showed expression of *Satb2,* which is expressed in the lower jaw (30), correlating with Osr1+ cells in the tongue MCT (Figure 2E-G).

Based on the expression pattern of *Osr1* (22, 31, 32), we mainly expected fibroblastic or mesenchymal cell identities. However, several clusters did not correspond to fibroblast or mesenchymal cells. Within them, cluster 14 represents a small subpopulation of Osr1+ cells expressing typical endothelial cell markers such as *Pecam1* (Figure 2H and S2F). Cluster 11 contains a subpopulation of Osr1+ cells with a macrophage signature. These cells highly express *Mrc1*, *Adgre1* or *Csf1r*, whereas genes expressed in committed LTis and LTi precursors *Cd4*, *Il7r* and *Cxcr5* remain absent (Figure 2H and S2G). Cells from cluster 8 contain a higher proportion of mitochondrial gene expression and a reduced expression of ribosomal genes as compared to other clusters (Figure S2H). Therefore, we considered them as a

damaged fraction of cells generated during the process of cell isolation. By contrast, Osr1+ cells in cluster 4 corresponded to proliferative cells as reflected by the higher expression of cell cycle genes relative to other clusters (Figure S2H). Within the cells corresponding to mesenchymal or fibroblastic cells but assigned to trunk and craniofacial regions, we found that cells in cluster 15 exclusively expressed *Vtn* (Figure 2H and I) and correlated with embryonic meningeal fibroblasts (33) (Figure 2J).

Of the Osr1+ trunk clusters, cluster 1 contains cells with a transcriptional profile enriched in extracellular matrix (ECM) markers, such as *Thsd4*, *Dpt* or *Col14a1* (Figure 2H, I, and S2I). Osr1+ cells abundantly expressed COL1 in the region of the aorta and esophagus (Figure 2K). Cluster 3 likely represented MCT fibroblasts of the trunk, which strongly express *Osr1* (22), given the expression of *Aldh1a3* and *Cited1* (eurexpress database, http://www.eurexpress.org) (Figure 2H, I, L and S2J). Cluster 6 exclusively expressed *Tnmd* and *Tppp3* and showed an enrichment in *Mfap5* expression, suggesting a tenocyte and tendon sheath fibroblast identity (34) (Figure 2H, I and S2K). Osr1+ cells were found in tendons marked by collagen XII and in tendon sheaths (Figure 2M). Besides, Osr1+ cells were found flanking the tendon attachment region of trunk muscles (Figure 2M). Cluster 7 was defined by exclusive expression of *Irx1* and an enrichment in ECM genes, such as *Lum*, *Dcn* and *Tnc* (Figure 2H, I and S2L). Embryonic skin transcriptome data (35) suggested *Osr1* and *Irx1* as specific markers for skin fibroblasts. In line, we found co-expression of TNC and *Osr1* in the E13.5 dermis (Figure 2N). Cluster 9 enclosed a heterogenous population of cells with a diverse transcriptional profile including *Acta1*+ atrial myofibroblasts and *Wt1*/*Upk3b*+ epicardial/mesothelial cells (Figure 2H, I and S2M). *Osr1* was highly expressed in the heart epicardial region at E13.5 (Figure 2O), and *Osr1* expression was reported in atrial cardiomyocytes (36). Of note, gene enrichment analysis using available embryonic scRNA-seq datasets (37) confirmed the identity for endothelial cells, macrophages and atrial myofibroblasts (Figure S2N). Other cell identities were in part discordant, suggesting that our data could contribute to define embryonic mesenchymal subpopulations.

Cluster 2 showed enriched expression of *Cdh18* and *Grm7*, which so far were not associated with specific mesenchymal cell types. Of note, cluster 2 showed the highest expression of chemokines *Cxcl13* and *Cxcl12* (Figure 2H and S2O). We provisionally named cluster 2 cells as Cdh18^{high} mesenchymal cells. Due to their high chemokine production within the Osr1+ cells, we next focused on this cluster possibly enriched in trunk mesenchymal LTo cells.

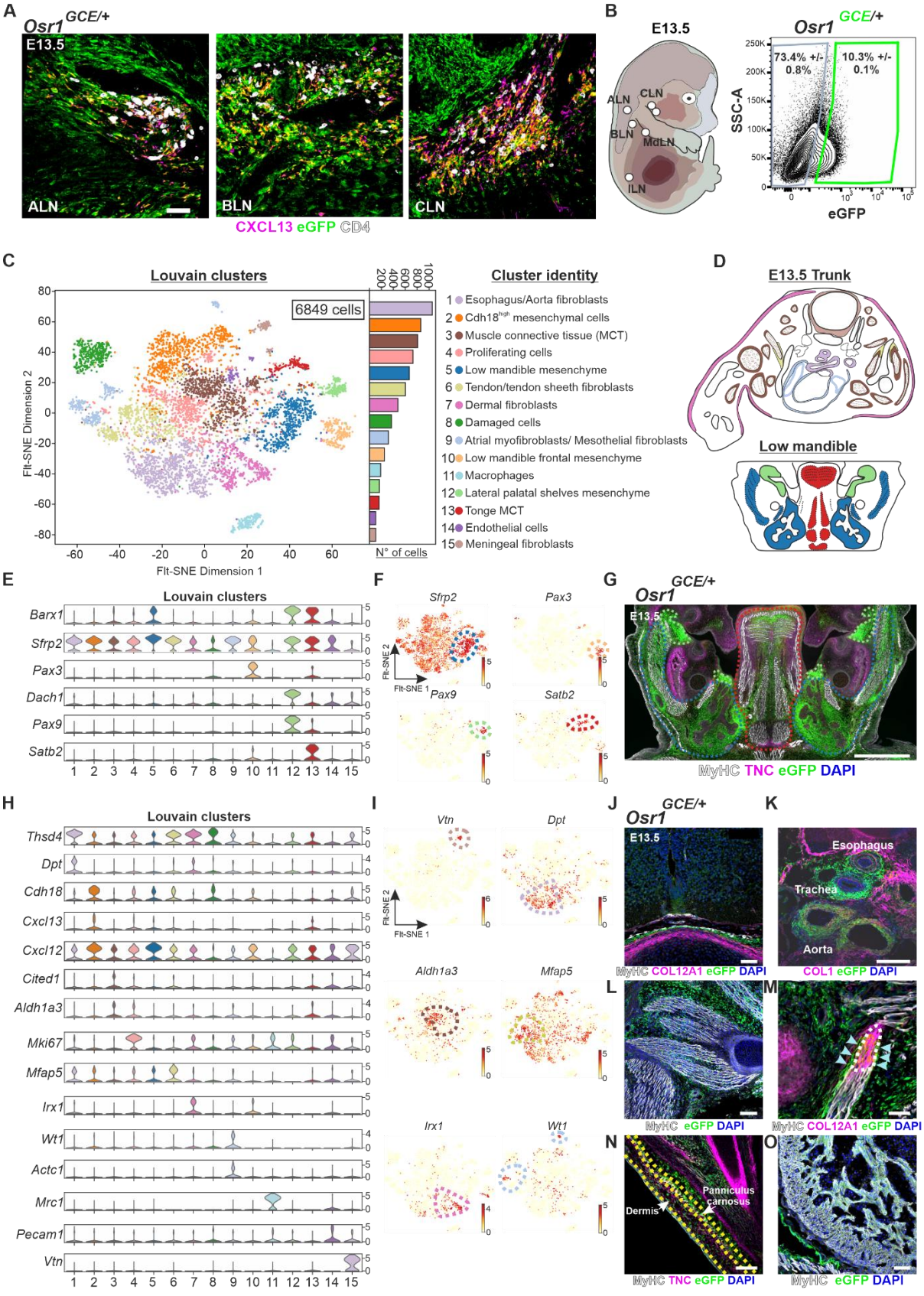

Figure 2. *Embryonic E13.5 Osr1 cell heterogeneity at the single-cell level.* ***(A)*** *Maximal intensity projection images of 35 µm cross-sections of E13.5 Osr1$^{GCE/+}$ peripheral LNs immunolabeled for CXCL13, CD4 and eGFP (Osr1).* ***(B)*** *FACS strategy to isolate Osr1 cells from E13.5 Osr1$^{GCE/+}$ embryos used for scRNA-seq.* ***(C)*** *FIt-SNE visualization of E13.5 Osr1 cells following Louvain cell clustering. Number of cells per cluster and assigned cell identities are indicated.* ***(D)*** *Schematic representation of putative cluster identity and tissue distribution of Osr1 cells of E13.5 trunk and low jaw in a cross-sectional view.* ***(E)*** *Violin plots of selected genes indicative of craniofacial identity depicting the distribution of gene expression within all cells per Louvain*

cluster. ***(F)*** *FIt-SNE visualization of cells expressing the indicated genes.* ***(G)*** *Osr1 expression in a cross-sectional view of the low jaw. Skeletal muscles are labeled for MyHC and dense connective tissue with TNC. Putative anatomical location of craniofacial clusters is labeled by colored dashed lines.* ***(H)*** *Violin plots of selected genes indicative of trunk identity depicting the distribution of gene expression within all cells per Louvain cluster.* ***(I)*** *FIt-SNE visualization of cells expressing the indicated genes for the trunk clusters.* ***(J-O)*** *Representative micrographs of E13.5 Osr1$^{GCE/+}$ embryos sections showing Osr1 expression at anatomical locations corresponding to putative Osr1+ subpopulations. Skeletal muscles were labeled for MyHC and connective tissue with COL1, COL12A1 or TNC. Immunofluorescences are representative images of at least 3 different embryos. Cells in scRNA-seq analysis are derived from a single E13.5 Osr1$^{GCE/+}$ embryo. In* ***(F, I)****, gene expression level in cells is depicted as log-transformed normalized counts. Scale bar represents in* ***(A)*** *50 µm,* ***(G)*** *600 µm and* ***(J-O)*** *100 µm. MdLN represents mediastinal LN.*

A common progenitor of white adipose tissue and mesenchymal LTos in the embryo

Cdh18^{high} mesenchymal cells of cluster 2 were enriched for Cxcl13+ cells (Figure 3A), indicative of enriched mesenchymal LTo identity. We thus focused on this cluster and performed Louvain subclustering for Cdh18^{high} mesenchymal cells, revealing 3 subclusters (Figure 3B). *Cxcl13* and also *Cxcl12* expression were increased in subclusters 2.1 and 2.2 compared to the subcluster 2.3 (Figure S3A). We therefore assumed mesenchymal LTos are mainly contained in subclusters 2.1 and 2.2. We used expression of *Ebf2* and *Igfbp5* to further distinguish these subclusters. *Ebf2* is a transcription factor found in adipogenic precursor cells (38) and is broadly expressed in Osr1+ cells (Figure S3B), however a higher expression within Cdh18^{high} cells was seen in subclusters 2.1 and 2.3 as compared to subcluster 2.2 (Figure 3C and S3B). EBF2 was highly abundant in Osr1+ trunk fibroblasts of the axillary region including MCT, putative mesenchymal LTos at the location of the brachial LN and surrounding interstitial mesenchyme. Osr1+ cells with a lower expression of EBF2 were located in the interstitium between aorta and esophagus of the mediastinal cavity (Figure 3C). Conversely, *Igfbp5* expression marked subcluster 2.2 (Figure 3D and S3B). IGFBP5 expression correlated with Osr1+ cells in the mediastinal cavity but not in the axillary region (Figure 3D). We thus termed the cells from subcluster 2.1 as peripheral mesenchymal LTos and the cells from subcluster 2.2 as mediastinal mesenchymal LTos.

Osr1+ cells in cluster 2.3 present an enrichment in genes involved in adipose tissue formation such as *Pparg, Fst*, *Sox9* and *Sox5* (39, 40) (Figures 3E, S3C). At E13.5, PPARG+ cells were identified in proximity to the cervical LN (Figure 3E). At E14.5, PPARG+ cells were found outside of the axillary and brachial LN anlagen and intermingled with CD45+ cells (Figure 3E and S3D). The mediastinal LN was devoid of PPARG+ cells (Figure S3E). *Pparg* expression was also found in subcluster 2.1 defined as peripheral mesenchymal LTos. In line, we observed CXCL13 and PPARG double positive cells in the axillary and brachial LN anlagen (Figure S3E) indicative of a bivalent population of interstitial cells. By comparing the transcriptional signatures of *Cdh18*^{high} subclusters (Figure S3F) with the defined identities of E18.5 and P3 stromal vascular fraction in the thoracic aorta-associated adipose tissue (41), we further confirmed an enriched adipocyte signature in subcluster 2.3 while subclusters 2.1 and 2.2 were enriched in a progenitor signature (Figure S3G).

Thus, at E13.5, Osr1+ *Cdh18^{high}* cells contain mesenchymal LTos and APCs in the trunk. This suggests that earlier Osr1+ cells may represent bipotential progenitors giving rise to white adipocytes and mesenchymal LTos. To assess this, we performed lineage tracing of E11.5 Osr1+ progeny until 18.5. Osr1 descendants were found in E18.5 LN mesenchymal stroma and as adipocytes in adjacent fat pads of the axillary, brachial and cervical regions (Figure 3F). In line with the postnatal formation of visceral fat (42), we did not detect a fat pad associated with the mediastinal LN in E18.5 embryos (Figure 3F).

Taken together, we defined a *Cdh18^{high}* mesenchymal cell population in the E13.5 trunk containing progenitors of mesenchymal LTos in trunk and mediastinal cavity, and also adjacent WAT in the trunk (Figure S3H). Divergent transcriptional profiles of LTos located in mediastinal and axillary regions indicate heterogeneity of mesenchymal LTos depending on the anatomical location.

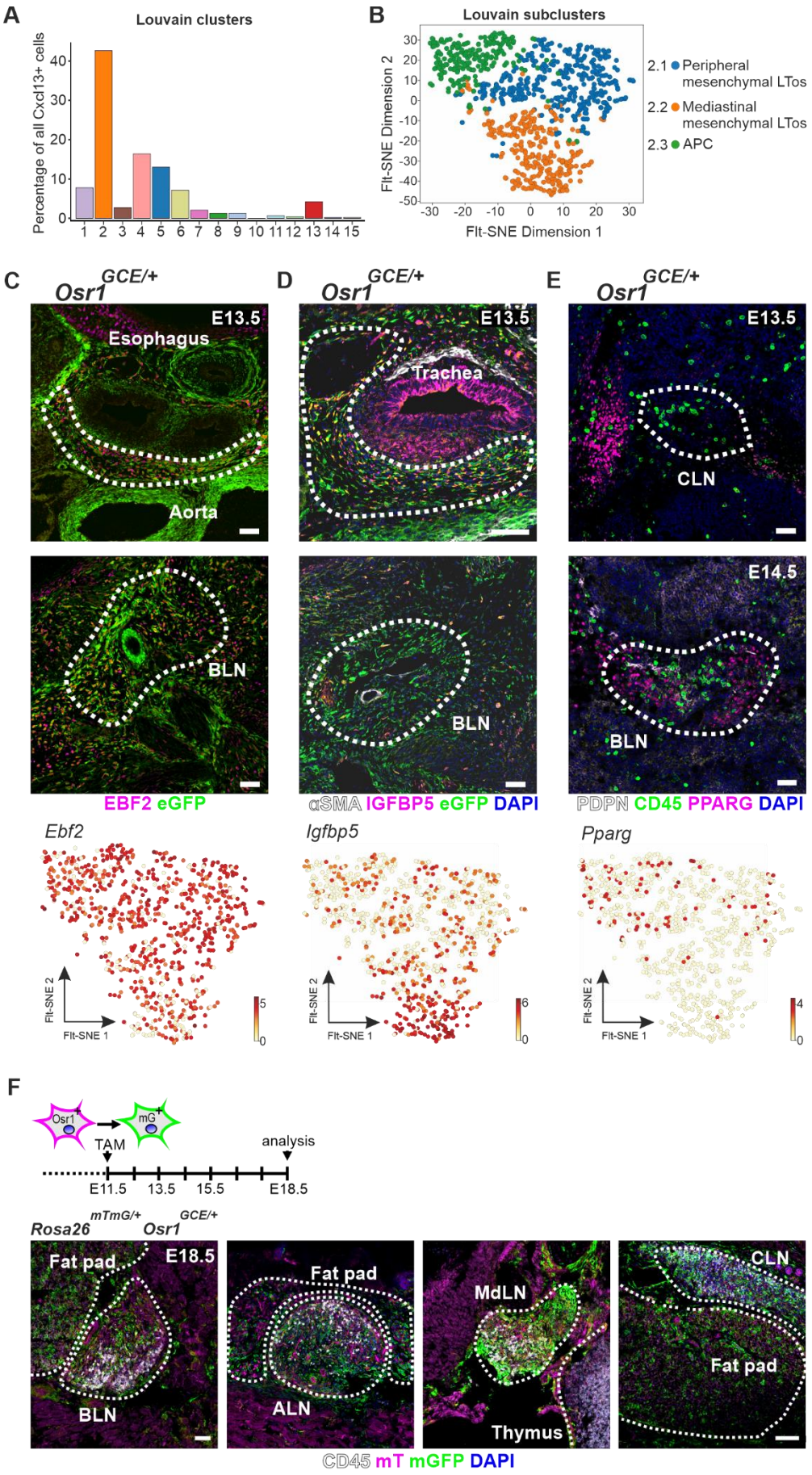

Figure 3. *Embryonic E13.5 Osr1 interstitial progenitors are a source of white adipocytes and mesenchymal LTos in the trunk.*
(A) *Bar plot depicting the percentage of Cxcl13 expressing cells within all Louvain clusters.* ***(B)*** *Fit-SNE visualization of Cdh18^{high}*

mesenchymal cells following Louvain cell subclustering with assigned cluster identities. ***(C, D)*** *Representative micrographs of E13.5 Osr1$^{GCE/+}$ mediastinal and axillary regions showing eGFP (Osr1), EBF2 or IGFBP5 co-expression. Below: FIt-SNE visualization of Ebf2 and Igfbp5* expressing cells*. Mural cells are labeled in* ***(D)*** *with αSMA.* ***(E)*** *Immunofluorescence of E13.5 and E14.5 Osr1$^{GCE/+}$ cervical and axillary regions showing PPARG+ fat pads in association with the LN anlage immunolabeled for CD45 and PDPN. Below: FIt-SNE visualization of Pparg expressing cells.* ***(F)*** *Schematic representation of tamoxifen injection for genetic lineage tracing; below: images of indicated LNs and associated fat pads showing Osr1 lineage (mGFP) contribution. CD45 cells demarcate peripheral and mediastinal LN anlage. Immunofluorescences are representative images of at least 3 different embryos. In* ***(C-E)****, gene expression level in cells is depicted as log-transformed normalized counts and dashed lines represent regions of interest. Scale bar represents in* ***(C-E)*** *50 µm and in* ***(F)*** *50 µm (BLN) and 100 µm (CLN).*

Cxcl13+ cell heterogeneity defines a functional niche in the LN anlage

Additionally to cluster 2, Cxcl13+ cells were also found in other clusters, e.g. in the craniofacial clusters, indicating a more heterogenous population of mesenchymal LTos (Figures 3A and 4A). Intriguingly, CXCL13 protein abundance itself was heterogeneous in different LN anlagen at E13.5 and E14.5 (Figure S4A). Thus, in order to resolve Cxcl13+ cell heterogeneity, we next analyzed our scRNA-seq dataset from the perspective of all *Cxcl13* expressing cells. Cell cycle effects were regressed out to also include cells in the proliferative cluster 4. Louvain subclustering of the 476 cells with a detectable *Cxcl13* expression from all clusters (203 *Cxcl13*+ cells from cluster 2 and 273 *Cxcl13*+ cells from other Louvain clusters) divided them into four subclusters (Figure 4B). Based on the expression of key genes (Figure S4B, C) such as *Barx1*, subcluster 1 was assigned with a craniofacial identity representing *Cxcl13*+ cells in low mandible mesenchyme (main cluster 5). *Cxcl13*+ subcluster 1 cells were therefore termed craniofacial mesenchymal LTos. Craniofacial mesenchymal LTos cells presented a higher content of ECM genes such as *Lum*, *Col25a1* or *Dcn* compared to other subclusters (Figure S4B, C). In line, cervical LN anlagen showed higher abundance of LUM protein, which was not detected or low in trunk and mediastinal LNs (Figure 4C).

Cxcl13+ cells in subclusters 2 and 3 shared a similar transcriptional profile to peripheral and mediastinal mesenchymal LTos (Figure S4B, C) and were identified by the expression of EBF2 and IGFBP5 (Figure 4D, E). Axillary brachial and mediastinal LNs showed abundant EBF2 protein expression, which was hardly present in the cervical LN (Figure 4D and S4D). As expected, an IGFBP5 enrichment was only found in the mediastinal cavity (Figure 4E).

The fourth subcluster of Cxcl13+ cells was enriched in the mural cell marker *Acta2* (43) (Figure 4B). These cells, which we termed mural LTos, also show an enriched expression of the chemokines *Ccl11* and *Ccl2* (Figure S4B, C). Immunolabeling confirmed expression of CXCL13 in ACTA2+ cells surrounding blood vessels of all LNs (Figure 4F), thus validating their mural cell identity. We note that co-expression of CXCL13 and ACTA2 was exclusively found in mural cells in LN anlagen, suggesting a specific mural cell identity in these regions.

Surprisingly, we also noticed expression of CXCL13 in a small proportion of LECs labelled by PROX1 or LYVE1 (Figure 4G and S4E). Similar to *Cxcl13*+ mural cells, expression of CXCL13 and PROX1 in LECs was only found in lymph vessels of the LN anlage. Consistently, *Cxcl13* transcripts were mainly detected in Osr1+ cells isolated by FACS and at lower levels in CD31+ PDPN+ LECs, but not in CD31+ PDPN- BECs (Figure 4H).

Altogether, subclustering of all Osr1+/Cxcl13+ cells in combination with *in situ* immunolabeling establish that embryonic mesenchymal LTos comprise a heterogeneous population of cells exhibiting specific transcriptional profiles depending on the anatomical location. Our results are complementary to recent data that highlights mesenchymal heterogeneity in E17.5 LNs (44) and indicates that E13.5 Osr1 mesenchymal LTos represent an earlier mesenchymal population with high CXCL13 expression. Of note, CD34 is expressed only at low levels in E14.5 mesenchymal LTos (Figure S4F,G). Finally, some LECs and mural cells in the LN anlage are specified to accessory LTos expressing the chemokine CXCL13.

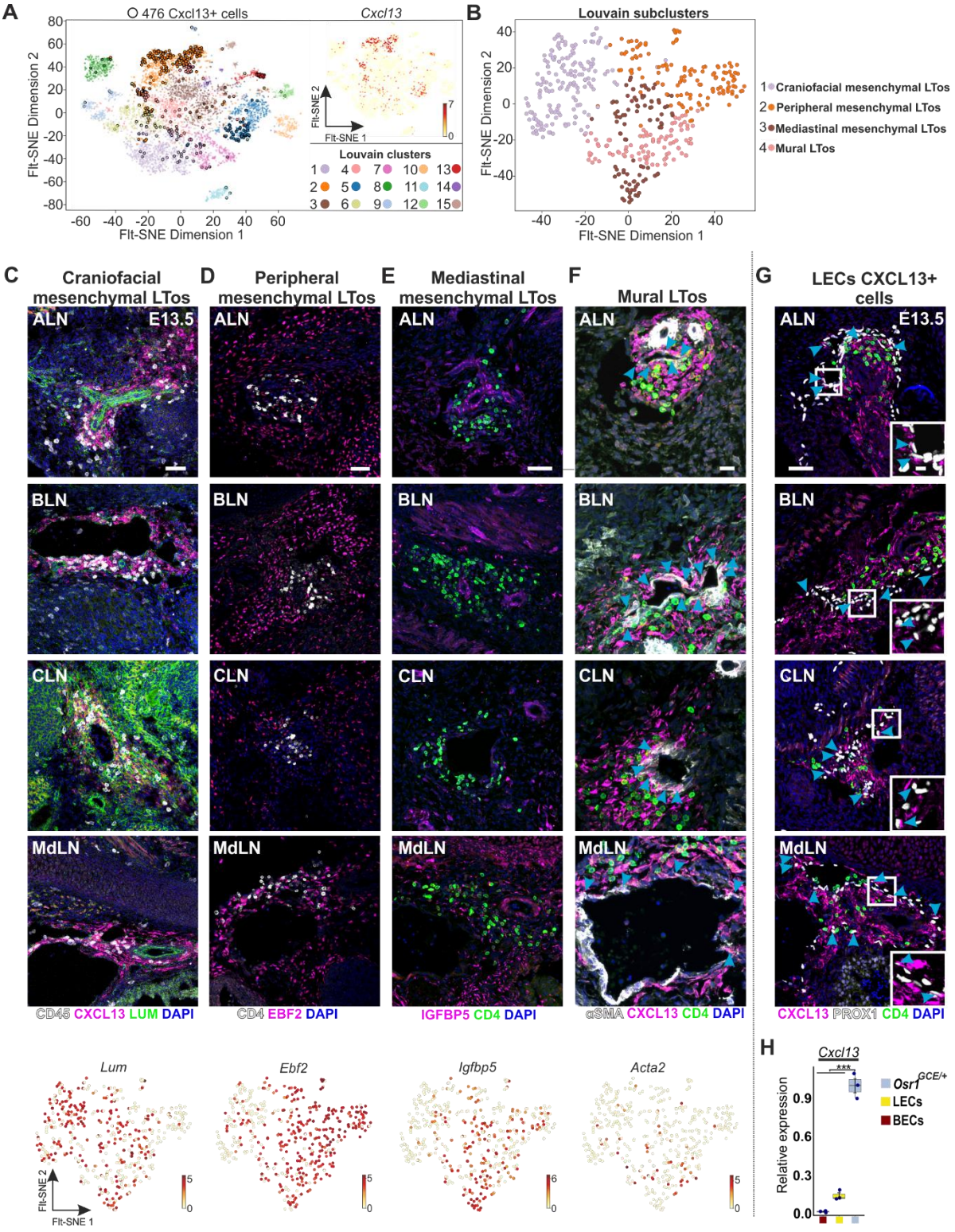

Figure 4. *Cxcl13 defines a functional niche in the LN anlage.* ***(A)*** *FIt-SNE visualizations of all Osr1+ cells highlighting the distribution of Cxcl13+ cells within Louvain clusters. Right: Cxcl13 expression in all Louvain clusters.* ***(B)*** *FIt-SNE visualization of Cxcl13+ cells following Louvain subclustering with the assigned cluster identity.* ***(C-G)*** *Representative micrographs of E13.5 Osr1$^{GCE/+}$ cross-sections of axillary, brachial, cervical, and mediastinal LNs immunolabeled for LUM, EBF2, IGFBP5 or ACTA2. LTis were labeled for CD45 or CD4, mesenchymal LTos for CXCL13, and LECs for PROX1. Below, FIt-SNE visualization of Lum, Ebf2, Igfbp5 and Acta2 in Cxcl13+ cell subclusters. In* ***G****, boxed regions are shown as higher magnification in the corner.* ***(H)*** *Relative expression of Cxcl13 transcripts in FACS isolated E13.5 BECs, LECs and Osr1+ (Osr1$^{GCE/+}$) cells. Immunofluorescence images are representative of at least 3 different embryos. In* ***(A, C-F)****, gene expression level in cells is depicted as log-*

*transformed normalized counts. Scale bar represents in **(C-E)** 50 µm, in **(F)** 20 µm and in **(G)** 50 µm and 10 µm (boxed region). In H, *** represents p< 0.001 and n=3. P values were obtained from one-way ANOVA with Dunnett´s post-hoc comparison.*

Osr1 is essential for LTi attraction to LN primordia, mesenchymal LTo commitment and LN-associated lymphatic vasculature assembly

We then asked whether *Osr1* is necessary for LTo specification and function. Homozygous knock-out of *Osr1* (*Osr1*$^{GCE/GCE}$) led to an arrest in LN initiation for PLNs (cervical, axillary, brachial, inguinal, jugular) and impaired LN initiation for mesenteric LNs (mediastinal and renal), hence all LNs that can be identified at E14.5 (Figure 5A and S5A). CD4+ cells were not attracted at all or were highly reduced. Interestingly, concomitant to the defective attraction of CD4+ cells, the lymphatic vasculature network of the LN anlagen was strongly impaired, with only few PDPN-high lymphatic vessels surrounding CD4+ cells in all LNs analyzed (Figure 5A and S5A). The absence of *Osr1* did not affect primary lymphoid organ development, as thymus formation was not impaired (Figure S5B), and normal spleen development has been previously reported in *Osr1*$^{GCE/GCE}$ embryos (45). *Osr1*$^{GCE/GCE}$ LN areas showed normal cellularity compared to controls and reduced proliferation of eGFP+ cells was observed in the cervical region, but not in other LNs (Figure S5C).

To bypass *Osr1*$^{GCE/GCE}$ embryo lethality at E14/15 due to heart defects (45), we generated a conditional *Osr1* allele (*Osr1*$^{fl/fl}$) from the previously described *Osr1*$^{LacZ/+}$ line (46) (Figure S5D). We used the *Prrx1-Cre* line mediating recombination in lateral plate mesoderm-derived mesenchymal cells (47). Recombination of *Rosa26*$^{mTmG/+}$ or *Osr1*$^{fl/fl}$ loci visualized by mGFP or eGFP, respectively, demonstrated *Prrx1*$^{Cre/+}$ activity in limb, limb girdle and mediastinal region including the ALN and BLN, and low activity in the CLN region (Figure S5E, F). In line, axillary and brachial LNs were not formed or highly impaired in E16.5 *Osr1*$^{fl/fl}$ *Prrx1*^{Cre} embryos, while cervical LNs formed normally (Figure 5B). In the axillary LN anlage, PDPN immunofluorescence demonstrated absence of associated lymphatic vasculature in E16.5 *Osr1*$^{fl/fl}$ *Prrx1*^{Cre} embryos (Figure 5B). *Osr1*$^{fl/fl}$ *Prrx1*^{Cre} embryos do not show edema, no embryonic or postnatal lethality was observed. This demonstrates that the defects in LTi recruitment and lymphatic vessel formation due to the loss of *Osr1* were not merely due to a developmental delay or global effects as edema appearing in Osr1$^{GCE/GCE}$ embryos.

Disrupted early LTi recruitment pointed to an aberrant commitment of mesenchymal LTo progenitors due to the loss of *Osr1*. To assess this, we first examined CXCL13 expression in the E13.5 LN anlage. CXCL13 protein was almost absent in peripheral axillary, brachial, and cervical LNs of E13.5 *Osr1*$^{GCE/GCE}$ embryos (Figure 5C) and reduced in renal LNs (Figure S5G). In line, *Cxcl13* expression was decreased in E13.5 *Osr1*$^{GCE/GCE}$ cells isolated by FACS (Figure 5D). We note that residual CXCL13 signal in the *Osr1*$^{GCE/GCE}$ LN anlage was mainly found in Osr1-GFP+ cells (Figure S5H), suggesting that Cxcl13/CXLC13 expression not exclusively depends on *Osr1*. In addition, *Cxcl12* expressed in all mesenchymal LTos, and *Ccl11* expressed in mural LTos, were also downregulated in E13.5 *Osr1*$^{GCE/GCE}$ cells, while *Ccl2* expressed in mural LTos was unaltered (Figure 5D and S5I, J). Although CXCL12 and CCL11 are capable of attracting LTis *in vitro* (12), and CXCL12 has a function in B cell migration (48, 49), a specific role in LN initiation *in vivo* has not been tested yet. Therefore, we examined LN initiation in embryos deficient for the CXCL12 main receptor CXCR4 (*CXCR4*$^{KO/KO}$) (50). CD4+ LTi accumulation was reduced in axillary, brachial and mediastinal LNs, whereas cervical LNs appeared to form normally (Figure 5E). Contrary to *Osr1*$^{GCE/GCE}$ embryos, we did not observe any impairment in LN lymphatic vasculature formation in E14.5 *CXCR4*$^{KO/KO}$ embryos (Figure 5E and S5K).

We conclude that *Osr1*-deficient mesenchymal progenitors are arrested in their early commitment to CXCL13+ mesenchymal LTos. Furthermore, mesenchymal LTos not only rely on CXCL13 for LTi attraction, as CXCL12/CXCR4 signaling is required for proper LTi recruitment to the LN anlage. Finally,

lack of *Osr1* in mesenchymal cells resulted in impaired formation of lymphatic vasculature in the LN anlage.

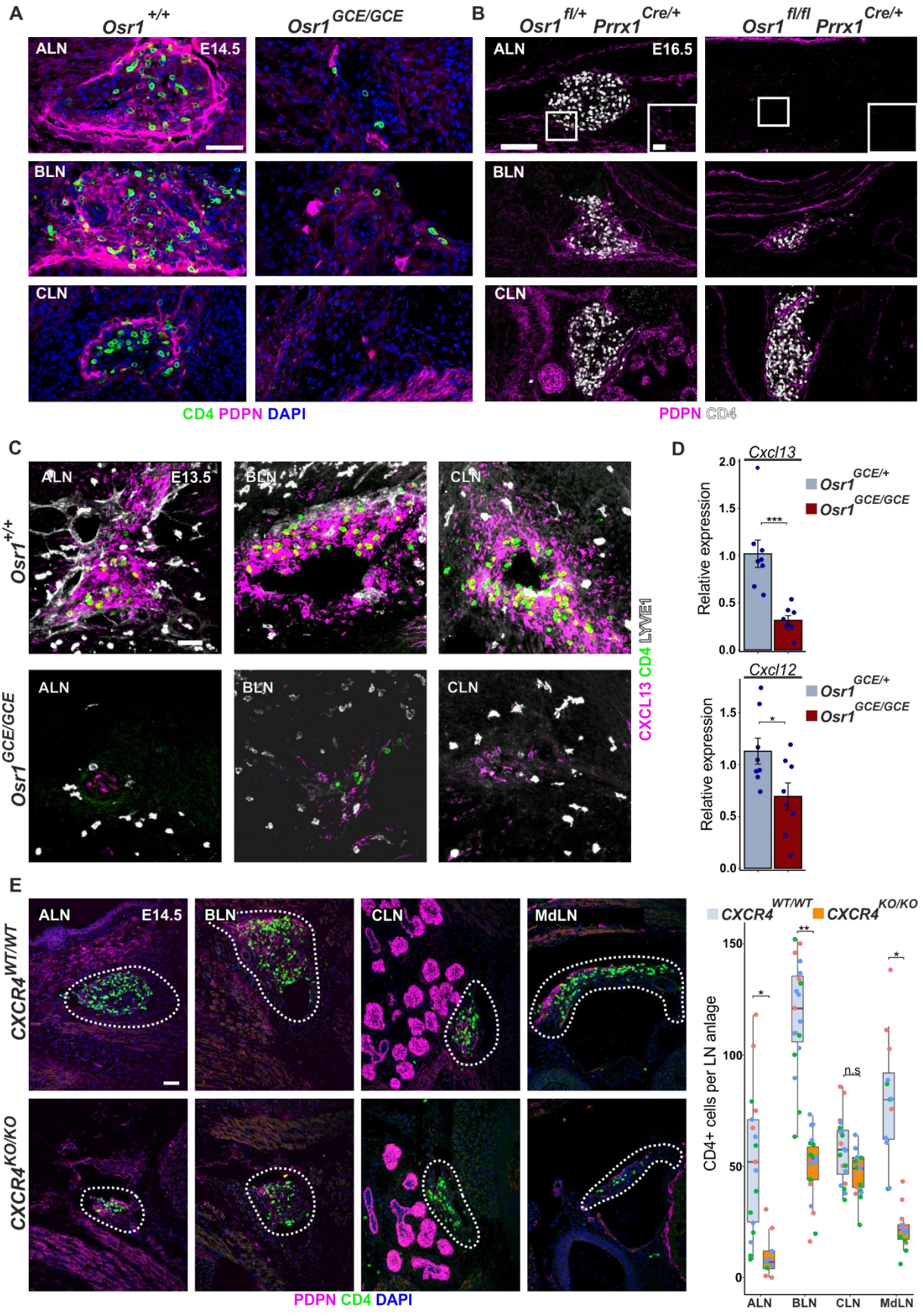

Figure 5. *Osr1+ mesenchymal cells orchestrate LTi accumulation and lymphatic vessel assembly in the LN anlage.* ***(A)*** *Representative micrographs of peripheral LN anlagen in E14.5 Osr1$^{+/+}$ and Osr1$^{GCE/GCE}$ embryos using anti CD4, PDPN and LYVE1 antibodies.* ***(B)*** *Representative images of LN anlagen in E16.5 Osr1$^{fl/+}$ Prrx1^{Cre} and Osr1$^{fl/fl}$ Prrx1^{Cre} embryos labeled for CD4 and PDPN. Lack of associated lymphatic vasculature in the ALN is shown as higher magnification at the right.* ***(C)*** *Maximal intensity projection depiction of 35 µm peripheral LNs sections of E13.5 Osr1$^{+/+}$ and Osr1$^{GCE/GCE}$ embryos labeled for CXCL13.*

LTis were labeled for CD4 and LECs for LYVE1. ***(D)*** *RT-qPCR for Cxcl13 and Cxcl12 in FACS isolated Osr1-GFP+ cells from E13.5 $Osr1^{GCE/+}$ and $Osr1^{GCE/GCE}$ embryos (n=8).* ***(E)*** *Representative images of peripheral and mediastinal LNs of E14.5 $CXCR4^{WT/WT}$ and $CXCR4^{KO/KO}$ embryos labeled for CD4 and PDPN. Dashed lines demarcate LN anlagen. At the right, quantification of CD4+ cells in LN anlagen per section is shown (n=3). Dot color represents measurements from different embryos. Immunofluorescence images have been captured from at least 3 independent experiments. Scale bar in (**A**) 50 µm, in (**B**) 100 µm and in (**C, E**) 50 µm. (**D, E**) Error bar represents s.e.m. and * p<0.05, ** p<0.01, *** p<0.001 or n.s not significant. P values were obtained from student's t-test.*

Mesenchymal retinoic acid signaling is required for LTo commitment

In the current view of LN initiation, Cxcl13 expression is triggered by RA secretion from neurons at the site of the LN primordium (12). However, transcriptome analysis of Osr1+ cells (22) showed robust expression of *Aldh1a2* encoding the main RA producing enzyme during development, which was decreased in $Osr1^{GCE/GCE}$ cells. Conversely, expression of *Cyp26b1* encoding the enzyme cytochrome P450 26B1 catabolizing all-trans RA was increased in $Osr1^{GCE/GCE}$ cells. This suggests that Osr1+ cells may themselves be a source and modulator of RA signaling. We first analyzed ALDH1A2 expression from E12.5 until E19.5 on tissue sections. High expression of ALDH1A2 was detected in meningeal and epicardial fibroblasts (Figure S6A), in line with previous reports (33, 51, 52), validating antibody fidelity. ALDH1A2 expression was observed at E12.5 in the axillary LN region in venous-associated mesenchymal LTos (Figure 6A and S6B). From this stage until E15.5, ALDH1A2 expression was restricted to mesenchymal LTos intermingling with CD45+ cells in peripheral and mesenteric LN anlagen (Figure 6A and S6C). ALDH1A2 expression decreased at late fetal stages and at E19.5 in the axillary LN only few cells expressed ALDH1A2 (Figure 6A). Comparing *Aldh1a2* expression between Osr1+ cells, BECs, LECs and CD45+ cells separated by FACS suggested that Osr1+ cells are the major source of RA production in the LN anlage (Figure 6B). Expression of ALDH1A2 in mesenchymal cells at E13.5 was corroborated by PDGFRα staining (Figure S6D). Next, we confirmed *Aldh1a2* downregulation and *Cyp26b1* upregulation in E13.5 $Osr1^{GCE/GCE}$ cells by RT-qPCR (Figure 6B). Despite the mild reduction of *Aldh1a2* mRNA expression, ALDH1A2 protein was severely reduced in LN anlagen of E13.5 $Osr1^{GCE/GCE}$ embryos, and almost absent in ALN and BLN (Figure 6C). Importantly, motoneurons in the vicinity of most PLNs and mesenteric LNs did not express high levels of ALDH1A2 (Figure 6C). Expression of ALDH1A2 in TUJ1+ motoneurons was in fact only observed close to the BLN (Figure 6C and S6E). These motoneurons however did not show reduced ALDH1A2 in E13.5 $Osr1^{GCE/GCE}$ embryos (Figure 6C and S6E). These results suggest that in LN anlagen RA is mainly produced by mesenchymal LTos and that mesenchymal RA signaling may be severely impaired in $Osr1^{GCE/GCE}$ embryos.

RA activates *Cxcl13* expression *in vitro* (12), suggesting that lack of RA signaling in $Osr1^{GCE/GCE}$ embryos causes failed mesenchymal LTo commitment. However, a link between RA receptor (RAR) inactivation and CXCL13 expression *in vivo* during LN initiation has not been established. We first treated pregnant mice with the RAR inhibitor BMS493. At E13.5, expression of RA target *Rarb* was decreased after BMS493 treatment, but not that of other RAR genes (Figure S6F). A reduction specifically of *Cxcl13*, but not other chemokine genes, was confirmed in E13.5 embryos treated with BMS493 (Figure S6F). CXCL13 protein abundance and CD4+ cell accumulation were severely decreased in axillary, brachial and mediastinal LNs of E13.5 BMS493 treated embryos (Figure S6G). To specifically inactivate RA signaling in mesenchymal cells, we analyzed $RARαDN^{fl/fl}$ $Prrx1^{Cre/+}$ embryos (53). At E13.5, these embryos show a reduced expression of CXCL13 and a concomitant reduced CD4+ LTi accumulation in LN anlagen (Figure 6D). This establishes that RA signaling in mesenchymal LTos is required for initial *Cxcl13* expression and thus LTo commitment and LN initiation.

As both, absence of *Osr1* or reduction of RA signaling in LTos disrupts *Cxcl13* expression, we analyzed whether *Cxcl13* activation by RA (12) *in vitro* depends on *Osr1*. Although robust upregulation of *Rarb* confirmed efficacy of RA treatment, RA stimulation triggered only a very mild upregulation of *Cxcl13* in $Osr1^{GCE/+}$ cells, which was, however, abrogated in $Osr1^{GCE/GCE}$ cells (Figure 6E), suggesting that *Osr1* is

required for RA-mediated *Cxcl13* activation. Interestingly, we observed a fast downregulation of *Cxcl13* expression *in vitro* (Figure 6F). We hypothesized that downregulation of *Cxcl13* expression might be caused by a lack of 3-dimensional cell environment, and cultivated *Osr1*$^{GCE/+}$ cells in embryoid bodies. This, however, also led to rapid downregulation of *Cxcl13* (Figure S6H). In 24h embryoid bodies, lentiviral infection using an Osr1-FLAG construct did not stimulate *Aldh1a2* expression. In addition, RA stimulation and/or Osr1-FLAG lentiviral infection, neither separately or in conjunction, could sustain *Cxlc13* expression (Figure S6H), despite robust *Rarb/Osr1* upregulation (Figure S6H).

We next tested whether loss of *Osr1*, in addition to LTi attraction, also affected LTi differentiation. Flow cytometric analysis showed that CD45+ cell abundance in the liver of E13.5 *Osr1*$^{GCE/GCE}$ was comparable to control littermates (Figure S6I). However, we measured a reduction of CD45+ cells in tissue comprising PLNs in E13.5 *Osr1*$^{GCE/GCE}$ embryos (Figure S6I). To investigate if CD45+ cell reduction in PLNs was accounted exclusively by a LTi reduction, we performed flow cytometric analysis of the CD45+/CD3- CD11b-cells containing LTi precursors and mature LTis in PLN enriched tissue. We detected no alteration in IL7Rα+ CD4+ LTis or IL7Rα+ CD4- LTi precursors in E14.5 *Osr1*$^{GCE/GCE}$ mice compared to controls (Figure 6G). In addition, *Rorc* and *Cd4* transcript levels were unchanged in both CD45+ isolated cells from E13.5 *Osr1*$^{GCE/GCE}$ peripheral tissues and whole E13.5 tissues from BMS493-treated embryos (Figure S6J). These results suggest that lack of mesenchymal ALDH1A2 in *Osr1*$^{GCE/GCE}$ embryos did not affect LTi precursor differentiation into CD4+ LTi cells.

We conclude that mesenchymal LTos are the main producers of RA in most LN anlagen, and that RA production is affected by loss of *Osr1*. Mesenchymal RA signaling controls in part CXCL13 expression dependent on *Osr1*, but not the expression of other chemokines involved in LN initiation. Finally, our results in *Osr1*$^{GCE/GCE}$ and BMS493-treated embryos suggest that mesenchymal RA is only involved in mesenchymal LTo commitment and not in LTi differentiation.

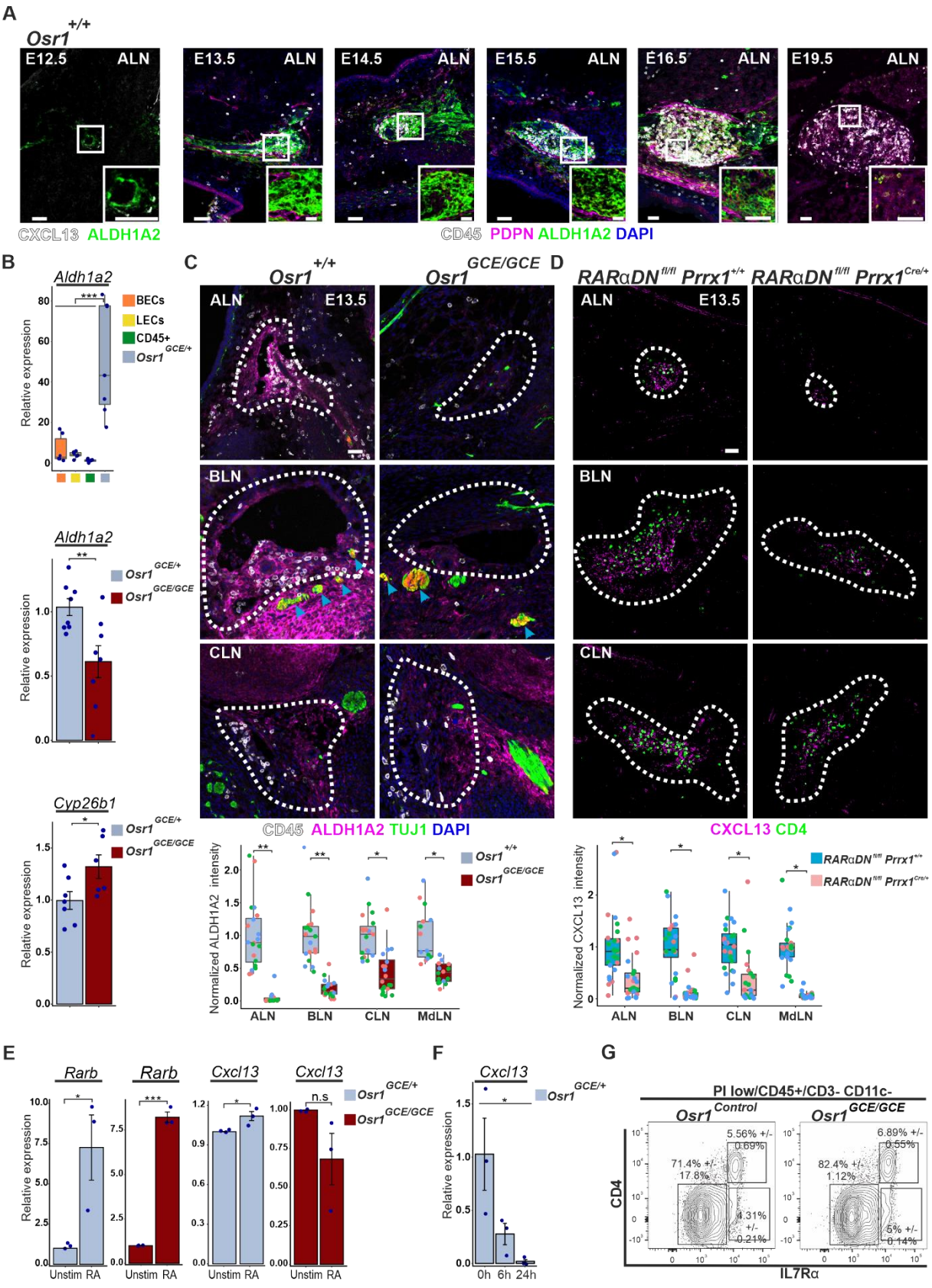

Figure 6. *Osr1+ LTis are a source of RA, and RA signaling is required for mesenchymal LTo commitment.* ***(A)*** *Representative Immunofluorescence images of the axillary region at indicated stages showing ALDH1A2 expression by mesenchymal LTos. At E12.5 in the axillary region first CXCL13+ cells are found in the proximity of the thoracic artery co-expressing ALDH1A2. LTis are labeled for CD45 and LECs with PDPN. Boxed regions are shown as higher magnifications.* ***(B)*** *RT-qPCR of Aldh1a2 expression in FACS isolated E13.5 Osr1+ cells, BECs, LECs or CD45+ cells. Below: Osr1 E13.5 Osr1$^{GCE/GCE}$ FACS isolated cells present a reduction in Aldh1a2 and an increase in Cyp26b1 transcripts assessed by RT-qPCR (n=6-8).* ***(C)*** *Representative micrographs of ALN, BLN, CLN and mediastinal LNs of Osr1$^{+/+}$ and Osr1$^{GCE/GCE}$ embryos labelled for ALDH1A2, CD45 for immune*

cells and TUJ1 for motoneurons. Motoneurons only show ALDH1A2 expression at the BLN, which was not decreased in Osr1$^{GCE/GCE}$ embryos (blue arrowheads). Below, normalized ALDH1A2 intensity in the LN anlage quantified on sections ***(D)*** *CXCL13 expression and CD4+ LTi accumulation is reduced in LNs of E13.5 RARαDN$^{fl/fl}$ Prrx1$^{Cre/+}$ embryos as compared to controls. Below, normalized CXCL13 intensity in the LN anlage quantified on sections (n=3).* ***(E)*** *Stimulation of E13.5 Osr1$^{GCE/+}$ and Osr1$^{GCE/GCE}$ cells isolated by FACS with all-trans retinoic acid (100 nM). A very mild upregulation of Cxcl13 transcripts is seen after 6h of retinoic acid activation only in E13.5 Osr1$^{GCE/+}$cells, whereas a robust Rarβ upregulation is seen in Osr1$^{GCE/+}$ and Osr1$^{GCE/GCE}$ cells (n=3).* ***(F)*** *Analysis of Cxcl13 expression measured by RTqPCR in E13.5 Osr1+ isolated by FACS from LNs enriched regions (n=3).* ***(G)*** *Flow cytometry to discriminate LTi precursors (CD4-) and mature LTis (CD4+) from E14.5 Osr1 controls and Osr1$^{GCE/GCE}$ peripheral tissue. CD45+/CD3- CD11c-/Il7Rα+ CD4+ cells were not reduced in Osr1$^{GCE/GCE}$ embryos (n=3-4). Immunofluorescence images were captured from at least 3 independent experiments. Dot colors in graphs of (**C**, **D**) represent measurements from different embryos. Scale bar in (**A**) 50 µm and in (**C**, **D**) 50 µm. In (**B**, **C, D, E and F**) error bar represents s.e.m. and * p< 0.05, ** p< 0.01, *** p< 0.001 or n.s nor significant. In (**B** and **F**), P values were obtained from one-way ANOVA with Dunnett´s post-hoc comparison, or by using a student's t-test (Osr1^{GCE} vs Osr1$^{GCE/GCE}$). In (**C, D** and **E**), P values were obtained from student's t-test. In (**G**) data are shown as a percentage of the mean and as a +/- percentage of the s.e.m.*

LN initiation requires the combined action of mesenchymal LTos and lymphatic vasculature

Expression of CXCL13 and its receptor CXCR5 are essential for the formation of most peripheral LNs, however cervical and mesenteric LNs still develop in single KO mutant embryos (17, 54). In *Osr1$^{GCE/GCE}$* deficient embryos, initiation is arrested in all PLNs and mesenteric LNs are strongly impaired, thus additional factors must contribute to LN initiation. CCL21, which is expressed in lymphatic endothelial cells, attracts LTis via its receptor CCR7 (12). Intriguingly, *Osr1* knockout embryos present defects in LN lymphatic vasculature.

CCL21 is produced exclusively by lymphatic vasculature independent of their position in the embryo (Figure S7A). At E14.5, lymphatic vasculature impairments also resulted in an interrupted production of the chemokine CCL21 in E14.5 *Osr1$^{GCE/GCE}$* peripheral and mesenteric LN anlagen (Figure 7A). To validate a synergistic function of LECs expressing CCL21 and mesenchymal LTos expressing CXCL13, we analyzed early LN initiation in E13.5 *Cxcl13$^{KO/KO}$* compared to *Cxcr5/Ccr7* double KO mutants. Surprisingly, Cxcl13 KO embryos showed an initial normal accumulation of LTis in peripheral LNs at E13.5 (Figure 7B). At E14.5 axillary and brachial LNs in *Cxcl13$^{KO/KO}$* did not contain LTis (Figure S7B) suggesting a failure in LTi retention. This phenotype is maintained during development and *CXCL13$^{KO/KO}$* embryos at E18.5 do not develop axillary and brachial LNs and show strongly reduced cervical LNs (Figure S7C). In contrast, the combined lack of *Cxcr5* and *Ccr7*, thus disrupting CXCL13 and CCL21 signaling simultaneously, led to complete absence of LTi recruitment to all LNs at E13.5 (Figure 7B and S7D) thus phenocopying lack of *Osr1*.

Collectively, our data indicate that the initial recruitment of LTis is not solely dependent on CXCL13, but needs the coordinated action of lymphatic vasculature and mesenchymal LTos as a general mechanism in the formation of PLNs and mesenteric LNs.

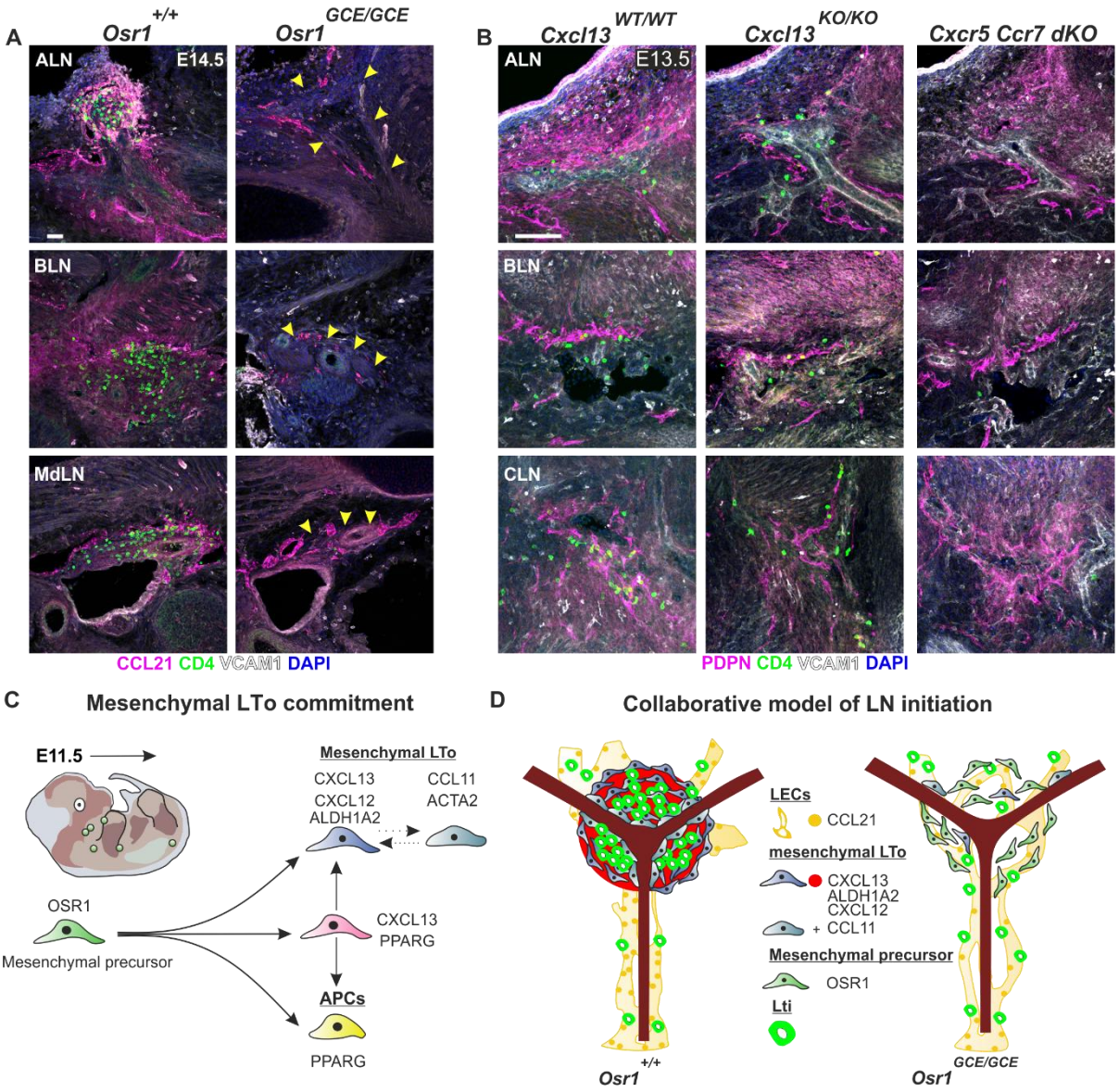

Figure 7. *Mesenchymal cells and LECs cooperate in LN initiation.* ***(A)*** *Maximal intensity projection of 35-µm sections showing defective lymphatic vasculature in E14.5 Osr1$^{GCE/GCE}$ ALN, BLN and mediastinal LN with an interrupted CCL21 expression (arrowheads). CD4 and VCAM1 label LTis and blood vasculature.* ***(B)*** *Immunofluorescence of 35 µm sections of ALN, BLN and CLN in E13.5 CXCL13$^{WT/WT}$, CXCL13$^{KO/KO}$ and CXCR5/CCR7 double KO mice. Note normal CD4+ cell accumulation in E13.5 CXCL13$^{KO/KO}$ but no CD4+ cell accumulation in CXCR5 CCR7 double KO. PDPN and VCAM1 label lymphatic and blood vasculature.* ***(C)*** *Schematic representation of mesenchymal LTo commitment and* ***(D)*** *Osr1 function in LN initiation. Immunofluorescence images were captured from at least 3 independent experiments. Scale bar represents in* ***(A)*** *50 µm and in* ***(B)*** *100 µm.*

Discussion

In mice, LN initiation starts at E12.5 (2, 5), however visualization and analysis of LN anlagen earlier than E14.5 in the literature are rare, leaving cell types involved in the first attraction of LTis poorly characterized. We show that Osr1+ mesenchymal cells represent the first defined precursor of mesenchymal LTos and are an early origin for the three known types of adult mesenchymal LN cells: FDCs, TRCs, and MRCs. Quantitative analysis showed only a partial contribution of Osr1 progenitors to these cell pools, however our analysis might underappreciate the contribution of Osr1 cells as (i) Osr1+ cells were tamoxifen-labelled only in a very short time frame thus probably not encompassing all LTo progenitors during the early phase of LN initiation; and (ii) possible low recombination efficacy of the Osr1-CreERt2 allele (compare Osr1-eGFP expression at E14.5/16.5 and lineage mGFP labeling at E15.5 in Figures 1A and S1E). Recently characterized subpopulations of mesenchymal stromal cells (26) are probably also derived at least in part from Osr1+ embryonic cells, as embryonic Osr1+ traced cells are broadly distributed in the LNs, however this remains to be tested. Interestingly, *Osr1* expression remains active in the medullary region of adult LNs and PPs, indicating a yet undefined function in adult LNs.

Embryonic and adult APCs have been proposed as a source of LN stromal cells (11). However, a common embryonic progenitor for both tissue types has not been addressed yet. By disentangling E13.5 Osr1+ cell heterogeneity via genetic lineage tracing and scRNA-seq, we defined a new Osr1+/Cdh18^{high} mesenchymal subpopulation in the trunk with enriched expression of *Cxcl12* and *Cxcl13*. Further bioinformatic and *in vivo* expression analysis subdivided these cells into adipogenic progenitors and mesenchymal LTos. Genetic lineage tracing of E11.5 Osr1+ cells confirmed their bifurcated potential thus strongly suggesting a common cellular origin for mesenchymal LN stromal cells and adipogenic progenitors (Figure 7C). Of note, some cells in axillary and brachial LN anlagen displayed a bivalent signature co-expressing CXCL13 and PPARG at E14.5. This suggests that, at least in these LNs, progenitors of LN-associated WAT and mesenchymal LTos are committed during the same developmental time frame including a phase of cellular plasticity towards either lineage (Figure 7C). Activation of the Ltβr signaling pathway in mesenchymal LTos is crucial for their late differentiation and inhibits adipocyte differentiation of isolated APCs (11). However, early mesenchymal LTo commitment occurs independently of this signaling cascade (12, 15). This indicates that commitment of APCs at E13.5 might also occur independently of Ltβr signaling and that Ltβr signaling may rather be necessary to maintain mesenchymal LTo identity at later stages by continuous suppression of adipogenic fate.

Formation of LNs at diverse locations of the body requires commitment of mesenchymal precursors to LTos in different tissue environments. In line, the formation of ectopic lymphoid tissue under fingolimod treatment in mice highlights LN emergence as an adaptive process (20). Thus, cellular adaptation in different cell types or even the reprograming of differentiated cells under certain conditions might be necessary. We show that Osr1+/CXCL13+ mesenchymal LTos in the cervical, peripheral and mediastinal region presented distinct transcriptional signatures, which resemble transcriptional profiles of mesenchymal cells in designated anatomical locations. They also expressed a localized ECM, which might contribute to LN diversity and local adaptation. Complementary to recent data (44) and Cxcl13-EYFP lineage contribution (20), Osr1+/CXCL13+ mesenchymal LTos represent an early precursor population with low expression of CD34 suggesting that E17.5 populations of mesenchymal precursors have a common origin in CXCL13+ cells. In line with transcriptional heterogeneity found in Osr1/CXCL13+ mesenchymal LTos, E17.5 mesenchymal subpopulations are heterogeneously distributed within inguinal, brachial and mesenteric LNs (44).

In the current view of LN initiation, localized production of RA by motoneurons adjacent to the LN anlage was proposed to activate *Cxcl13* expression in mesenchymal LTos (12). However, motoneurons

are broadly distributed along the embryo and RA production by neurons does not follow a pattern similar to LN distribution in the body (55-57). We show that (i) at several LN anlagen motoneurons do not express ALDH1A2, while (ii) in all LN anlagen mesenchymal LTos express high levels of ALDH1A2, suggesting LTos themselves are the predominant producers of RA in the area of LN formation. Furthermore, in *Osr1*$^{GCE/GCE}$ embryos, motoneurons in the vicinity of brachial LNs show normal ALDH1A2 expression, nevertheless CXCL13 expression and brachial LN formation are severely impaired, altogether arguing against a significant role of neural-derived RA and pointing to mesenchymal cells as a main RA source.

Osr1-deficient LTos show reduced expression of *Aldh1a2*/ALDH1A2 and increased expression of *Cyp26b1,* which very likely limits local mesenchyme-derived RA availability impinging on CXCL13 expression. In line, inhibition of RA signaling either globally (BMS493 treatment) or specifically in mesenchymal cells (*RARαDN*$^{fl/fl}$ *Prrx1*$^{Cre/+}$) led to both reduction of *Cxcl13* expression and LTi attraction, demonstrating the crucial role of RA signaling in mesenchymal LTo commitment and LN initiation. Neither BMS493 treatment or lack of RA signaling nor lack of *Osr1* completely abrogated CXCL13 production by mesenchymal LTos, suggesting additional players in the control of *Cxcl13* expression. In line with this, we surprisingly found a dynamic downregulation of *Cxcl13* after embryonic cell isolation and *in vitro* culture, which could not be recovered by lentiviral Osr1-FLAG overexpression and/or RA signaling activation. Of note, lack of local mesenchymal RA production in *Osr1*$^{GCE/GCE}$ embryos did not affect LTi differentiation, in line with a dependence of the last differentiation step from LTi precursors to mature LTis on maternal RA (14).

In summary, our data suggest that motoneuron-derived RA is not involved in LN initiation but demonstrate a crucial role for mesenchymal RA signaling in LN initiation, challenging the current model of LN initiation.

The transcription factor *Osr1* has been involved in the formation of several organs, cell-autonomously controlling mesenchymal cell differentiation, directly regulating expression of ECM genes or transcription factors such as *Sox9* or*Tcf7l2* and the chemokine *Cxcl12* (22, 25, 58-60) or acting in a non-cell autonomous manner influencing cell behavior (22). Despite being required for *Aldh1a2* and *Cxcl13* expression *in vivo*, we could not establish a direct regulation of both genes by *Osr1*.

The critical function of *Osr1* in mesenteric and peripheral LN initiation in the embryo cannot be only explained by reduced CXCL13 expression observed in *Osr1*$^{GCE/GCE}$ embryos. In the absence of CXCL13 or its receptor CXCR5, cervical LNs and mesenteric LNs still develop (26, 52). Furthermore, our analysis of *Cxcl13*$^{KO/KO}$ embryos at E13.5 revealed normal initial LTi attraction to all LN anlagen. Mesenchymal LTos showed high expression of *Cxcl12* and *Ccl11*, encoding two chemokines attracting LTis *in vitro* (12). Indeed, we showed here that the CXCL12 receptor CXCR4 is required for proper attraction of LTis during LN initiation in peripheral and mesenteric LNs. However, cervical LNs in *CXCR4*$^{KO/KO}$ embryos develop normally. These results point to a differential requirement for chemokine factors in the initiation of cervical, mesenteric, and peripheral LNs. We show that in the LN anlage an additional subpopulation of Osr1+/CXCL13+ mural cells acquired mesenchymal LTo functions. Osr1+/CXCL13+ mural cells remain attached to the vascular vessels and express αSMA, and also showed expression of *Ccl11* and *Ccl2*. Whether these chemokines contribute to, and are required for, LN initiation at specific locations remains to be tested. In addition, a small proportion of lymphatic endothelial cells at the LN anlage acquired CXCL13 expression *in situ*. Thus, the production of CXCL13 in different cell types together with the assistance of other chemokines might create a multifactorial microenvironment necessary for LTi recruitment during development.

Mesenchymal cells are an unappreciated actor in lymphatic vasculature formation during development and in adult tissues. We reveal a critical function for Osr1+ mesenchymal cells in lymphatic vasculature

assembly in all LNs. Lymphatic vessels play an essential role collecting CD4+ cells from peripheral tissues and conducting them to the LN anlage (21). In addition, lymphatic vasculature produces a potent LTi-attracting chemokine, CCL21 (12). *Cxcr5/Ccr7dKO* embryos recapitulate the global defects seen in *Osr1* mutants demonstrating a requirement for combined CXCL13 and CCL21 signaling. This suggests that the combined action of lymphatic vasculature and mesenchymal LTos via CXCL13 and CCL21 is a general mechanism in LTi recruitment necessary for LN initiation across divergent anatomical locations. In $Osr1^{GCE/GCE}$ embryos, both, disrupted lymphatic vessel assembly and subsequent impaired CCL21 expression in the prospective LN region might contribute to defects in all LNs we observed, thus exacerbating the defects seen in $Cxcl13^{KO/KO}$ embryos. This places the mesenchymal transcription factor *Osr1* upstream of two processes crucial for LN initiation, orchestrating both mesenchymal LTo commitment and formation of LN-associated lymphatic vasculature. Of note, the initial expression of CXCL13 by mesenchymal LTos and CCL21 expression by lymphatic vasculature are independent of LTβR signaling (12, 15).

Current views of LN initiation are based on the isolated function of mesenchymal or endothelial organizer cells. Together, our data substantially revise the identity and function of mesenchymal cells involved in LN initiation. They unify the divergent actual views of LN initiation adapting the prevailing paradigm of LN initiation to a new model that incorporates the pivotal role of mesenchymal cells in lymphatic vessel formation to achieve LTi attraction at the LN anlage.

Acknowledgements

This work was funded by the Deutsche Forschungsgemeinschaft (DFG; grant VA 1272/1-1) and the Freie Universität Berlin. We are gratefully to Andrew P. McMahon (Keck School of Medicine of USC, USA) and Andreas Kispert (Hannover Medical School, Germany) for providing $Osr1^{GCE}$ and $R26^{mTmG}$ mouse lines. We thank Carmen Birchmeier and Ines Lahmann (Max Delbrück Center for Molecular Medicine, Berlin, Germany) for providing $Cxcr4^{+/-}$ mice and technical support. We gratefully thank Caroline Bräuning (Max Delbrück Center for Molecular Medicine, Berlin, Germany) for assisting scRNA-seq experiments. We thank Uta Marchfelder and Erwin Weiß (Max Planck Institute for Molecular Genetics, Germany) for FACS sorting support. We thank Stefan Mundlos, Nobert Brieske and Thorsten Mielke for their support (Max Planck Institute for Molecular Genetics, Germany). We also thank Petra Knaus (Freie Universität, Berlin) for the support with lentiviral infection.

Author contributions:

Conceptualization P.V.G and S.S. P.V.G performed the majority of experiments and data collection. G.C, M.G and S.P-K performed data collection. C.G-T supervised FACS experiments. C.F and S.Sa. supervised the scRNA-seq procedure. M.O performed scRNA-seq data analysis. G.C, S.T and U.H provided reagents and mouse embryos. G.C performed BMS493 treatment. Formal analysis and interpretation were performed by P.V.G, M.O and S.S. P.V.G, M.O, U.H and S.S wrote the manuscript.

All authors critically reviewed and approved the final version of the manuscript.

Methods

Animals

Mice were maintained in an enclosed, pathogen-free facilities, and experiments were performed in accordance with European Union regulations and under permission from the Landesamt für Gesundheit und Soziales (LaGeSo) Berlin, Germany (Permission numbers ZH120, G0346/13, G0240/11, G0268-16) and the ethics committee of the Institute Pasteur (CETEA) (licence 2015-008). Mouse lines were described previously; *Osr1*^{GCE} (23), *Prrx1*^{Cre} (47), *R26R*^{mTmG} (61), *Osr1*^{LacZ} (46), *Cxcr4*$^{+/-}$ (50), CXCR5 (18), CXCL13 (breeding pairs derived from Jackson Laboratories, Bar Harbor, ME, USA), CCR7 (62), and CXCR5/CCR7 DKO (63).

To transform the *Osr1*$^{LacZ/+}$ locus in a *Osr1*$^{fl/fl}$ locus, we bred *Osr1*$^{LacZ/+}$ animals with animals expressing ubiquitous flippase recombinase (64). Then, we bred *Osr1*$^{fl/fl}$ animals with *Prrx1*^{Cre} animals (47) to achieve constitutive excision of *Osr1* exon2 in mesenchymal cells of most peripheral LNs, but not affecting *Osr1* function in heart development (45, 65) (a schematic representation of the *Osr1* locus is depicted in figure S5C).

Tamoxifen and Progesterone administration for Osr1^{+} cell lineage tracing

As we described previously (22), tamoxifen (Sigma Aldrich) was dissolved in a 1:10 ethanol/sunflower oil mixture. For embryonic lineage tracing, we bred *R26R*$^{mTmG/mTmG}$ females to *Osr1*$^{GCE/+}$ males. Pregnant females were injected with 150 µl of a 20 mg mL^{-1} tamoxifen stock. Tissues were collected at E18.5.

For lineage tracing experiments inducing at embryonic stages and analysing adult SLNs, we bred *Osr1*$^{GCE/+}$ females to *R26R*$^{mTmG/mTmG}$ males. To ameliorate negative effects of tamoxifen during delivery a mixture of 60 µl was injected intraperitoneally to the pregnant female containing 20 mg ml^{-1} tamoxifen and 16,6 mg ml^{-1} Progesterone (Sigma Aldrich). Adult tissues were collected at 8-12 weeks of age.

For perinatal lineage tracing, new born *Osr1*$^{GCE/+}$; *R26R*$^{LacZ/+}$ pups were injected subcutaneously into the neck fold with 25 µl of a 3 mg ml^{-1} tamoxifen stock. Adult tissue was collected at 12 weeks of age. For successive injections, only 1 injection was performed in 24h.

BMS493 treatment

To inhibit retinoic acid signalling *in vivo*, we used the pan-RAR inverse agonist BMS493 (Tocris, 3509). As described in (66), pregnant females were injected intraperitoneally with 10 mg kg^{-1} of BMS493. BMS493 was dissolved in dimethyl sulfoxide (DMSO, Sigma Aldrich) at a concentration of 5 mg ml^{-1} and stored at -20 °C in tight cap tubes. Immediately prior injection, 200 µl sterile phosphate buffer (PBS) was added per 50 µl BMS493 aliquot. BMS493 and DMSO injections were performed every 12h as described in schematic representation.

Retinoic acid treatment

To activate retinoic acid signalling *in vitro*, cells were treated with all-trans retinoic at a concentration of 100 nM (Sigma Aldrich) added to cell culture medium.

Tissue preparation

Embryonic tissues were fixed in 4% PFA for 2h on ice or overnight at 4°C in case eGFP has to be detected after antigen retrieval. Tissues were dehydrated in two steps using 15% and 30% (w/v) sucrose (Roth) solutions before O.C.T. (Sakura) cryo-embedding in a chilled ethanol bath. Embryonic tissue was

sectioned at 12 or 35 µm thickness. Adult LNs were collected, freed from remaining fatty tissue and fixed in 4% PFA solution at 4°C overnight. Adult tissue was sectioned at 12 µm thickness.

Immunolabelling

Cryo-sections were warmed up for at least 30 minutes at room temperature (RT). Antigen retrieval was performed for the antibodies ALDH1A2, LUM and PPARG. In this case, sections were shortly washed with PBS and subsequently immerse in 1x Target Retrieval Solution (Dako) pH 6. Heat-induced epitope retrieval was achieved using a steamer (IHCWorld) for 30 min. Retrieval solution was thoroughly rinsed out with PBS. Sections were blocked with 5% (v/v) Horse Serum (Vector Laboratories) in 0.1% (v/v) Triton X-100 (Sigma Aldrich) PBS for 1h at RT. Primary antibodies dissolved in blocking solution were incubated at 4 °C overnight, followed by secondary antibody staining of 1h at RT. Antibodies used for these experiments are listed in supplementary tables 1 and 2. Specimens were counterstained with 5µg μL^{-1} 4',6-diamidino-2-phenylindole (DAPI; Invitrogen) and mounted with FluoromountG (SouthernBiotech).

Cell isolation and flow cytometry

For cell isolation of embryonic tissues, E13.5 *Osr1*$^{GCE/+}$ or *Osr1*$^{GCE/GCE}$ tissues were enriched in LNs dissecting the embryos from the axilla until the tongue and including the inguinal region. Embryonic tissue was minced using a small scissor in 1 ml high-glucose Dulbecco's modified eagle medium (DMEM, Pan Biotech) containing 10% foetal bovine serum (FBS, Pan Biotech) and 1% penicillin/streptomycin (P/S) solution. Further enzymatic digestion of the tissue was performed using 0,7 mg ml^{-1} of Collagenase (Collagenase A, Roche) in DMEM medium at 37 °C for 45 min. Antibody labelling (antibodies see supplementary table 3) was performed for 20 min on ice. For the isolation and FACS analysis of LTis and their precursors, LNs enriched tissues were dissected from E14.5 *Osr1*^{controls} and *Osr1*$^{GCE/GCE}$ embryos and treated as above described for E13.5 embryos. Antibody labelling (antibodies see supplementary table 3) was performed for 15 min at RT.

For stromal cell isolation of adult LNs, PLNs and mesenteric LNs from *Rosa26*$^{mTmG/+}$ *Osr1*$^{GCE/+}$ and *Rosa26*$^{mTmG/+}$ *Osr1*$^{+/+}$animals were dissected and shortly minced with a small scissor in 5 ml DMEM medium containing 10% FBS and 1% P/S. LNs were further enzymatic digested adding 0,8 mg ml^{-1} collagenase and 0,2 mg ml^{-1} Dispase II (Roche) for 45 min at 37 °C. Cell suspensions were collected by centrifugation at 400g for 8 min and washed with a solution containing PBS and 2% FBS. Cell suspension were enriched in stromal cells by depleting CD45+ hematopoietic cells using MACS microbeads (Miltenyi). For that, hematopoietic cells were bound to CD45+-microbeads (10µl/10^7 cells) and depleted using LS columns (Miltenyi). Unbound cell suspension was collected and used for further antibody labelling performed for 20 min on ice.

Before flow cytometry, cell suspensions were washed using a solution containing PBS, 0,4% FBS and 2 mM EDTA, collected by centrifugation at 300 g for 5 min and passed through a 35-µm cell strainer filter (BD Biosciences). To assess viability, cells were stained with propidium iodide (2 µg ml^{-1}, eBioscience) immediately before sorting or analysis.

Sorts and analyses were performed on a FACS Aria II and FACS Aria fusion (BD Biosciences). Data were collected using FACSDIVA software. Further analyses were performed using FlowJo 10 (FlowJo LLC) software. Sorting gates were defined based on unstained and fluorescence negative controls. Cells were collected into 400 µl high-glucose DMEM.

Lentiviral infection

Lentiviral particles were purchased from AMSBio (Abingdon, UK). For embryoid bodies infections, E13.5 C57Bl6 LNs enriched tissues were isolated as described above (Cell isolation and flow cytometry). 4 x 10^4 E13.5 cells were resuspended in pre-warmed growth medium (high glucose DMEM supplemented with 10% FBS) to a concentration of 1000 cells per µl. Osr1-FLAG virus particles were added to the cells in a multiplicity of infection of 1 and RNA was isolated 24 h after. Mouse embryonic fibroblast (MEFs) infections of E13.5 C57Bl6 cells were conducted as previously described (22) and achieved by spinoculation. Virus particles and cells were centrifuge for 60 min at 300 g before seeding.

Chromatin immunoprecipitation

Chromatin immunoprecipitation (ChIP) using E13.5 MEFs infected with Osr1-FLAG was performed as previously described (22). Briefly, cells were fixed with 1% formaldehyde (Sigma Aldrich) for 10 min. Chromatin cross-linking was quenched by adding 550 µl of 2.5 M Glycine. Next, cells were washed twice with DPBS and collected with a scratcher. After cell lysis, nuclei were collected in 900 µl sonication buffer and sonicated for 20 cycles in a Bioruptor (Biogenade). For ChIP, 30 µg sonicated chromatin was incubated with an anti-FLAG antibody under rotation at 4°C overnight. Protein G beads (Invitrogen) was added to the chromatin-antibody mixture and incubated under rotation at 4°C overnight. Dynabeads-antibody complex was isolated from the chromatin using vigorous shaking at 65°C for 30 min and further de-crosslinked overnight at 65°C. Proteins bound to the chromatin were removed with a treatment of 60 min at 55°C using Poteinase K (500mg/ml) and subsequently a treatment of 30 min at 37°C with RNase A (Sigma Aldrich). Genomic DNA used as an input was obtained using de-crosslinked chromatin without antibody pulldown. Primer sequences are provided in supplementary table.

Imaging

X-Gal staining of whole LNs were documented with a Zeiss SteREO Discovery V12 stereomicroscope. Confocal images of immunolabelled sections were taken using the confocal laser scanning microscope systems LSM710, LSM810 (Zeiss) or Leica DMi8 microscopes. Images were captured using Zen 2010 (Zeiss) and LAS Life System (Leica). For the quantifications shown in figures 5E, S5C, S5H, 6C, D and S6G, consecutive images of the LN region were selected leaving 12µm (1 section) between quantified images. ALDH1A2 and CXCL13 protein intensity on sections were quantified by the ImageJ algorithm "integrated density" as sum of pixels values in the LN anlage. In Figure S5C and H, percentage of Ki67/eGFP and eGFP/CXCL13 overlapping signals were obtained using the ImageJ tool image calculator-subtract. The percentage of overlapping signals were quantified by the ImageJ algorithm "integrated density".

Quantitative real-time PCR

Total RNA extraction from FACS isolated cells was performed using Direct-zol™ RNA MicroPrep and MiniPrep kits (Zymo Research) following manufacturer´s protocol. Reverse transcription was conducted using the M MuLV Reverse Transcriptase Kit (Biozym). Relative gene expression analyses were performed using GoTaq® qPCR kit (Promega) or Blue S´Green qPCR kit (Byozim) on a 7900HT Real Time PCR system or QuantStudio 7 Flex Real-Time-PCR-System (Applied Biosystems). Primer sequence information is provided in supplementary table 4. Data were acquired and analysed using SDS 2.0 and QuantStudio™ Real-Time PCR softwares (Applied Biosystems).

Droplet-based single-cell RNA-seq analysis

E13.5 *Osr1*$^{GCE/+}$ cells from LNs enriched tissues were isolated via FACS and 10,000 collected cells were run using the 10x Chromium (10x Genomics) system according to the manufacturer´s recommendations (Chromium Single Cell 3' chemistry V3 Kit). After generation of Gel Beads-in-Emulsion (GEM), cDNA was amplify in a thermal cycler using 10 cycles (98°C for 3 minutes, 98°C for 15 seconds, 63°C for 20 seconds and 72°C for 1 minute). The libraries were constructed performing a sample index PCR of 11 cycles (98°C for 45 seconds, 98°C for 20 seconds, 54°C for 30 seconds and 72°C for 20 seconds). Final libraries had a concentration of 17.1 ng/µl and 504 bp on average. Libraries were sequenced on an Illumina HiSeq 4000 device using the following read specifications: 8-bp index, 28-bp read 1 (16-bp barcode and 12-bp UMI), and 98-bp strand-specific read 2.

The ~58 M sequencing reads generated were mapped against the primary assembly of the mouse genome mm10, for which we included an additional synthetic sequence encompassing the eGFPCreERt2 and PGK-Neo cassettes corresponding to the Osr1^{GCE} allele, using the STARsolo algorithm from STAR v2.7.5c (67) (parameters: --solotype CB_UMI_Simple; --sjdbOverhang 97; --soloCBstart 1; --soloCBlen 16; --soloUMIstart 17; --soloUMIlen 12; --soloStrand Forward; --outSAMtype BAM SortedByCoordinate; --outMultimapperOrder Random; --outSAMattributes NH HI NM MD AS nM CR CB CY UR UB UY GX GN). The primary comprehensive gene model from the GENCODE vM25, excluding pseudogenes and small non-coding RNA genes but including the additional Osr1^{GCE} allele, was used as reference annotation (--sjdbGTFfile) and the 10X Chromium barcode whitelist v3 (3M February 2018) was provided for error correction and demultiplexing of cell barcodes (--soloCBwhitelist), while allowing multiple matches in whitelist with no more than one mismatched base (--soloCBmatchWLtype 1MM_multi). Following mapping, multi-mapped reads were extracted from the alignment map according to the NH tag using SAMtools v1.10 (68) and intersected against the gene annotation model using BEDtools bamtobed (parameters: -tag HI; -split) and intersect (parameters: -s; -wa; -wb; -loj) v2.29.2 (69). Multi-mapped reads that were found to overlap with a single gene were retrieved and merged with the uniquely-mapped reads, resulting in a total of ~48M aligned reads (83.1% of initial sequencing reads).

Next, reads mapped on genes were counted using featureCounts v2.0.1 (70) (parameters: -M; -s 1) according to first exon features (-t exon) and then transcript features (-t transcript) to include reads that originated from introns (pre-mRNAs) as well. Gene counting at the UMI level per cell was performed using STARsolo error-corrected barcodes and UMI-tools count v1.0.0 (71), while using the directional method to group reads per UMI with a maximum hamming distance of 1 (parameters: --extract-umi-method=tag; --umi-tag=UR; --cell-tag=CB; --method=directional; --per-gene; --per-cell). The resulting count matrix was then parsed to exclude low-quality cells (< 600 counts, < 500 genes and $\geq$ 10% mitochondrial counts) and sparse genes (expressed in < 0.05% cells, i.e. < 4 cells). The 6849 cells that remained after filtering, with a median number of counts per cell of 3473 and covering 21,412 genes for a median number of genes per cell of 1844 (Figure S2C), were further analyzed using Pegasus v1.0.0 (72). Gene counts were first normalized to 10^5 to obtain an identical sum per cell and scaled using a logarithmic transformation after adding a pseudocount of 1. The top 2000 genes with the highest variance were then selected for downstream analysis. Principal component analysis (PCA) was used to reduce the dimensionality of the data by computing 50 principal components (PCs). A *k*-nearest neighbors (kNN) graph was constructed from the 50 PCs by fixing the local neighborhood number at 100. Clustering was performed using the Louvain algorithm with a resolution set at 1.3 and the fast interpolation-based *t*-distributed stochastic neighbor embedding (FIt-SNE) on two dimensions was chosen for visualization with a perplexity of 30 and an early exaggeration of 12. Differential expression

analysis between Louvain clusters was performed using a Mann-Whitney *U* test and a q-value threshold (alpha) of 0.05 for significance.

To identify putative cell-type-specific gene markers, differentially expressed genes detected as being upregulated in each cluster were filtered out according to a percentage fold change of at least 2 between the percentage of expressing cells in a given cluster relative to all other clusters, resulting in a list of 7730 upregulated genes across all Louvain clusters. Hierarchical clustering of upregulated genes was performed by averaging their expression level across all cells for each cluster and by using the clustermap function from the Python package seaborn v0.11.0 (73) with the average linkage method and the correlation distance metric. Cell type enrichment analysis of Louvain clusters was assessed by comparing the upregulated genes detected for each cluster against the 2861 gene markers identified for the 38 cell types defined from E9.5-E13.5 mouse embryos (37). Statistical significance of marker gene overlaps was computed using a hypergeometric test followed by a false discovery rate (FDR) correction with the Benjamini-Hochberg method.

To further investigate the cell population corresponding to the Louvain cluster 2, the 860 cells contained exclusively within this cluster were analyzed using Pegasus v1.0.0 (72) by adjusting the following parameters: PCA was computed on the top 400 genes with the highest variance and 5 PCs; the number of nearest neighbors was fixed at 80 to construct the kNN graph; and the resolution was set at 0.5 for Louvain subclustering.

To explore the heterogeneity within the *Cxcl13*+ cell population, the 476 cells with at least 1 UMI count for *Cxcl13* were extracted. 203 (42.6%) cells were included in the Louvain cluster 2, while the 273 (57.4%) remaining cells were spread among the 14 other Louvain clusters except for the Louvain cluster 10. Analysis of these 476 *Cxcl13*+ cells was performed using Pegasus v1.3.0 (72). The 400 most highly variable genes were selected and PCA was computed on 5 PCs. To include the 78 (16.4%) *Cxcl13*+ cells contained within the Louvain cluster 4 of proliferative cells, cell-cycle scores were calculated based on the cell cycle genes defined in (74). Cell cycle effects were then regressed out on the PCs according to the predicted G1/S and G2/M phases. kNN graph was constructed from the regressed PCs by fixing the local neighborhood at 50 and a resolution of 0.7 was used for Louvain subclustering.

Statistical analysis

Student's t-test and one-way ANOVA with Dunnett´s post-hoc comparison were performed using Prism 8 (GraphPad) software. Error bars in all figures, including supplementary information, represent the mean ± standard error of the mean (s.e.m.). In figures 5E, 6C, 6D and S6G, student's t-test were performed using calculated averages from single measurements obtained from the same embryo.

Data availability

Raw fastq and count data from scRNA-seq sequencing experiments have been deposited in the Gene Expression Omnibus (GEO) database under the accession number GSE199851.

References:

1. van de Pavert SA, Mebius RE. New insights into the development of lymphoid tissues. Nat Rev Immunol. 2010;10(9):664-74.
2. van de Pavert SA. Lymphoid Tissue inducer (LTi) cell ontogeny and functioning in embryo and adult. Biomed J. 2021;44(2):123-32.

3. Mebius RE, Miyamoto T, Christensen J, Domen J, Cupedo T, Weissman IL, et al. The fetal liver counterpart of adult common lymphoid progenitors gives rise to all lymphoid lineages, CD45+CD4+CD3- cells, as well as macrophages. J Immunol. 2001;166(11):6593-601.
4. Simic M, Manosalva I, Spinelli L, Gentek R, Shayan RR, Siret C, et al. Distinct Waves from the Hemogenic Endothelium Give Rise to Layered Lymphoid Tissue Inducer Cell Ontogeny. Cell Rep. 2020;32(6):108004.
5. Krishnamurty AT, Turley SJ. Lymph node stromal cells: cartographers of the immune system. Nat Immunol. 2020;21(4):369-80.
6. Brendolan A, Caamano JH. Mesenchymal cell differentiation during lymph node organogenesis. Front Immunol. 2012;3:381.
7. Turley SJ, Fletcher AL, Elpek KG. The stromal and haematopoietic antigen-presenting cells that reside in secondary lymphoid organs. Nat Rev Immunol. 2010;10(12):813-25.
8. Castagnaro L, Lenti E, Maruzzelli S, Spinardi L, Migliori E, Farinello D, et al. Nkx2-5(+)islet1(+) mesenchymal precursors generate distinct spleen stromal cell subsets and participate in restoring stromal network integrity. Immunity. 2013;38(4):782-91.
9. Prados A, Kollias G, Koliaraki V. CollagenVI-Cre mice: A new tool to target stromal cells in secondary lymphoid organs. Sci Rep. 2016;6:33027.
10. Denton AE, Carr EJ, Magiera LP, Watts AJB, Fearon DT. Embryonic FAP(+) lymphoid tissue organizer cells generate the reticular network of adult lymph nodes. J Exp Med. 2019;216(10):2242-52.
11. Benezech C, Mader E, Desanti G, Khan M, Nakamura K, White A, et al. Lymphotoxin-beta receptor signaling through NF-kappaB2-RelB pathway reprograms adipocyte precursors as lymph node stromal cells. Immunity. 2012;37(4):721-34.
12. van de Pavert SA, Olivier BJ, Goverse G, Vondenhoff MF, Greuter M, Beke P, et al. Chemokine CXCL13 is essential for lymph node initiation and is induced by retinoic acid and neuronal stimulation. Nat Immunol. 2009;10(11):1193-9.
13. Eberl G, Marmon S, Sunshine MJ, Rennert PD, Choi Y, Littman DR. An essential function for the nuclear receptor RORgamma(t) in the generation of fetal lymphoid tissue inducer cells. Nat Immunol. 2004;5(1):64-73.
14. van de Pavert SA, Ferreira M, Domingues RG, Ribeiro H, Molenaar R, Moreira-Santos L, et al. Maternal retinoids control type 3 innate lymphoid cells and set the offspring immunity. Nature. 2014;508(7494):123-7.
15. Benezech C, White A, Mader E, Serre K, Parnell S, Pfeffer K, et al. Ontogeny of stromal organizer cells during lymph node development. J Immunol. 2010/03/20 ed2010. p. 4521-30.
16. Muller G, Hopken UE, Lipp M. The impact of CCR7 and CXCR5 on lymphoid organ development and systemic immunity. Immunol Rev. 2003;195:117-35.
17. Ansel KM, Ngo VN, Hyman PL, Luther SA, Forster R, Sedgwick JD, et al. A chemokine-driven positive feedback loop organizes lymphoid follicles. Nature. 2000;406(6793):309-14.
18. Forster R, Mattis AE, Kremmer E, Wolf E, Brem G, Lipp M. A putative chemokine receptor, BLR1, directs B cell migration to defined lymphoid organs and specific anatomic compartments of the spleen. Cell. 1996;87(6):1037-47.
19. Vondenhoff MF, van de Pavert SA, Dillard ME, Greuter M, Goverse G, Oliver G, et al. Lymph sacs are not required for the initiation of lymph node formation. Development. 2009;136(1):29-34.
20. Onder L, Morbe U, Pikor N, Novkovic M, Cheng HW, Hehlgans T, et al. Lymphatic Endothelial Cells Control Initiation of Lymph Node Organogenesis. Immunity. 2017;47(1):80-92 e4.
21. Bovay E, Sabine A, Prat-Luri B, Kim S, Son K, Willrodt AH, et al. Multiple roles of lymphatic vessels in peripheral lymph node development. J Exp Med. 2018;215(11):2760-77.
22. Vallecillo-Garcia P, Orgeur M, Vom Hofe-Schneider S, Stumm J, Kappert V, Ibrahim DM, et al. Odd skipped-related 1 identifies a population of embryonic fibro-adipogenic progenitors regulating myogenesis during limb development. Nat Commun. 2017;8(1):1218.
23. Mugford JW, Sipila P, McMahon JA, McMahon AP. Osr1 expression demarcates a multi-potent population of intermediate mesoderm that undergoes progressive restriction to an Osr1-dependent nephron progenitor compartment within the mammalian kidney. Dev Biol. 2008;324(1):88-98.

24. Zhou L, Liu J, Olson P, Zhang K, Wynne J, Xie L. Tbx5 and Osr1 interact to regulate posterior second heart field cell cycle progression for cardiac septation. J Mol Cell Cardiol. 2015;85:1-12.
25. Han L, Xu J, Grigg E, Slack M, Chaturvedi P, Jiang R, et al. Osr1 functions downstream of Hedgehog pathway to regulate foregut development. Dev Biol. 2017;427(1):72-83.
26. Rodda LB, Lu E, Bennett ML, Sokol CL, Wang X, Luther SA, et al. Single-Cell RNA Sequencing of Lymph Node Stromal Cells Reveals Niche-Associated Heterogeneity. Immunity. 2018;48(5):1014-28 e6.
27. Makarenkova HP, Meech R. Barx homeobox family in muscle development and regeneration. Int Rev Cell Mol Biol. 2012;297:117-73.
28. Zalc A, Rattenbach R, Aurade F, Cadot B, Relaix F. Pax3 and Pax7 play essential safeguard functions against environmental stress-induced birth defects. Dev Cell. 2015;33(1):56-66.
29. Lan Y, Ovitt CE, Cho ES, Maltby KM, Wang Q, Jiang R. Odd-skipped related 2 (Osr2) encodes a key intrinsic regulator of secondary palate growth and morphogenesis. Development. 2004;131(13):3207-16.
30. Sheehan-Rooney K, Palinkasova B, Eberhart JK, Dixon MJ. A cross-species analysis of Satb2 expression suggests deep conservation across vertebrate lineages. Dev Dyn. 2010;239(12):3481-91.
31. Stricker S, Brieske N, Haupt J, Mundlos S. Comparative expression pattern of Odd-skipped related genes Osr1 and Osr2 in chick embryonic development. Gene Expr Patterns. 2006;6(8):826-34.
32. Stricker S, Mathia S, Haupt J, Seemann P, Meier J, Mundlos S. Odd-skipped related genes regulate differentiation of embryonic limb mesenchyme and bone marrow mesenchymal stromal cells. Stem Cells Dev. 2012;21(4):623-33.
33. DeSisto J, O'Rourke R, Jones HE, Pawlikowski B, Malek AD, Bonney S, et al. Single-Cell Transcriptomic Analyses of the Developing Meninges Reveal Meningeal Fibroblast Diversity and Function. Dev Cell. 2020;54(1):43-59 e4.
34. Staverosky JA, Pryce BA, Watson SS, Schweitzer R. Tubulin polymerization-promoting protein family member 3, Tppp3, is a specific marker of the differentiating tendon sheath and synovial joints. Dev Dyn. 2009;238(3):685-92.
35. Sennett R, Wang Z, Rezza A, Grisanti L, Roitershtein N, Sicchio C, et al. An Integrated Transcriptome Atlas of Embryonic Hair Follicle Progenitors, Their Niche, and the Developing Skin. Dev Cell. 2015;34(5):577-91.
36. Hill MC, Kadow ZA, Li L, Tran TT, Wythe JD, Martin JF. A cellular atlas of Pitx2-dependent cardiac development. Development. 2019;146(12).
37. Cao J, Spielmann M, Qiu X, Huang X, Ibrahim DM, Hill AJ, et al. The single-cell transcriptional landscape of mammalian organogenesis. Nature. 2019;566(7745):496-502.
38. Wang W, Kissig M, Rajakumari S, Huang L, Lim HW, Won KJ, et al. Ebf2 is a selective marker of brown and beige adipogenic precursor cells. Proc Natl Acad Sci U S A. 2014;111(40):14466-71.
39. Gulyaeva O, Nguyen H, Sambeat A, Heydari K, Sul HS. Sox9-Meis1 Inactivation Is Required for Adipogenesis, Advancing Pref-1(+) to PDGFRalpha(+) Cells. Cell Rep. 2018;25(4):1002-17 e4.
40. Singh R, Braga M, Pervin S. Regulation of brown adipocyte metabolism by myostatin/follistatin signaling. Front Cell Dev Biol. 2014;2:60.
41. Angueira AR, Sakers AP, Holman CD, Cheng L, Arbocco MN, Shamsi F, et al. Defining the lineage of thermogenic perivascular adipose tissue. Nat Metab. 2021;3(4):469-84.
42. Kozak LP, Anunciado-Koza R. UCP1: its involvement and utility in obesity. Int J Obes (Lond). 2008;32 Suppl 7:S32-8.
43. Chang L, Noseda M, Higginson M, Ly M, Patenaude A, Fuller M, et al. Differentiation of vascular smooth muscle cells from local precursors during embryonic and adult arteriogenesis requires Notch signaling. Proc Natl Acad Sci U S A. 2012;109(18):6993-8.
44. Lenti E, Genovese L, Bianchessi S, Maurizio A, Sain SB, di Lillo A, et al. Fate mapping and scRNA sequencing reveal origin and diversity of lymph node stromal precursors. Immunity. 2022;55(4):606-22 e6.
45. Wang Q, Lan Y, Cho ES, Maltby KM, Jiang R. Odd-skipped related 1 (Odd 1) is an essential regulator of heart and urogenital development. Dev Biol. 2005;288(2):582-94.

956 46. Stumm J, Vallecillo-Garcia P, Vom Hofe-Schneider S, Ollitrault D, Schrewe H, Economides AN,
957 et al. Odd skipped-related 1 (Osr1) identifies muscle-interstitial fibro-adipogenic progenitors (FAPs)
958 activated by acute injury. Stem Cell Res. 2018;32:8-16.
959 47. Logan M, Martin JF, Nagy A, Lobe C, Olson EN, Tabin CJ. Expression of Cre Recombinase in the
960 developing mouse limb bud driven by a Prxl enhancer. Genesis. 2002;33(2):77-80.
961 48. Schmidt TH, Bannard O, Gray EE, Cyster JG. CXCR4 promotes B cell egress from Peyer's patches.
962 J Exp Med. 2013;210(6):1099-107.
963 49. Pikor NB, Morbe U, Lutge M, Gil-Cruz C, Perez-Shibayama C, Novkovic M, et al. Remodeling of
964 light and dark zone follicular dendritic cells governs germinal center responses. Nat Immunol.
965 2020;21(6):649-59.
966 50. Zou YR, Kottmann AH, Kuroda M, Taniuchi I, Littman DR. Function of the chemokine receptor
967 CXCR4 in haematopoiesis and in cerebellar development. Nature. 1998;393(6685):595-9.
968 51. Xavier-Neto J, Shapiro MD, Houghton L, Rosenthal N. Sequential programs of retinoic acid
969 synthesis in the myocardial and epicardial layers of the developing avian heart. Dev Biol.
970 2000;219(1):129-41.
971 52. Guadix JA, Ruiz-Villalba A, Lettice L, Velecela V, Munoz-Chapuli R, Hastie ND, et al. Wt1 controls
972 retinoic acid signalling in embryonic epicardium through transcriptional activation of Raldh2.
973 Development. 2011;138(6):1093-7.
974 53. Rosselot C, Spraggon L, Chia I, Batourina E, Riccio P, Lu B, et al. Non-cell-autonomous retinoid
975 signaling is crucial for renal development. Development. 2010;137(2):283-92.
976 54. Ohl L, Henning G, Krautwald S, Lipp M, Hardtke S, Bernhardt G, et al. Cooperating mechanisms
977 of CXCR5 and CCR7 in development and organization of secondary lymphoid organs. J Exp Med.
978 2003;197(9):1199-204.
979 55. Zhao X, Brade T, Cunningham TJ, Duester G. Retinoic acid controls expression of tissue
980 remodeling genes Hmgn1 and Fgf18 at the digit-interdigit junction. Dev Dyn. 2010;239(2):665-71.
981 56. Niederreither K, Fraulob V, Garnier JM, Chambon P, Dolle P. Differential expression of retinoic
982 acid-synthesizing (RALDH) enzymes during fetal development and organ differentiation in the mouse.
983 Mech Dev. 2002;110(1-2):165-71.
984 57. Vermot J, Schuhbaur B, Le Mouellic H, McCaffery P, Garnier JM, Hentsch D, et al. Retinaldehyde
985 dehydrogenase 2 and Hoxc8 are required in the murine brachial spinal cord for the specification of
986 Lim1+ motoneurons and the correct distribution of Islet1+ motoneurons. Development.
987 2005;132(7):1611-21.
988 58. Orgeur M, Martens M, Leonte G, Nassari S, Bonnin MA, Borno ST, et al. Genome-wide
989 strategies identify downstream target genes of chick connective tissue-associated transcription
990 factors. Development. 2018;145(7).
991 59. Liu H, Lan Y, Xu J, Chang CF, Brugmann SA, Jiang R. Odd-skipped related-1 controls neural crest
992 chondrogenesis during tongue development. Proc Natl Acad Sci U S A. 2013;110(46):18555-60.
993 60. Xu J, Liu H, Park JS, Lan Y, Jiang R. Osr1 acts downstream of and interacts synergistically with
994 Six2 to maintain nephron progenitor cells during kidney organogenesis. Development.
995 2014;141(7):1442-52.
996 61. Muzumdar MD, Tasic B, Miyamichi K, Li L, Luo L. A global double-fluorescent Cre reporter
997 mouse. Genesis. 2007;45(9):593-605.
998 62. Forster R, Schubel A, Breitfeld D, Kremmer E, Renner-Muller I, Wolf E, et al. CCR7 coordinates
999 the primary immune response by establishing functional microenvironments in secondary lymphoid
1000 organs. Cell. 1999;99(1):23-33.
1001 63. Hopken UE, Achtman AH, Kruger K, Lipp M. Distinct and overlapping roles of CXCR5 and CCR7
1002 in B-1 cell homing and early immunity against bacterial pathogens. J Leukoc Biol. 2004;76(3):709-18.
1003 64. Rodriguez CI, Buchholz F, Galloway J, Sequerra R, Kasper J, Ayala R, et al. High-efficiency deleter
1004 mice show that FLPe is an alternative to Cre-loxP. Nat Genet. 2000;25(2):139-40.
1005 65. Zhang KK, Xiang M, Zhou L, Liu J, Curry N, Heine Suner D, et al. Gene network and familial
1006 analyses uncover a gene network involving Tbx5/Osr1/Pcsk6 interaction in the second heart field for
1007 atrial septation. Hum Mol Genet. 2016;25(6):1140-51.

66. Comai GE, Tesarova M, Dupe V, Rhinn M, Vallecillo-Garcia P, da Silva F, et al. Local retinoic acid signaling directs emergence of the extraocular muscle functional unit. PLoS Biol. 2020;18(11):e3000902.
67. Dobin A, Davis CA, Schlesinger F, Drenkow J, Zaleski C, Jha S, et al. STAR: ultrafast universal RNA-seq aligner. Bioinformatics. 2013;29(1):15-21.
68. Li H, Handsaker B, Wysoker A, Fennell T, Ruan J, Homer N, et al. The Sequence Alignment/Map format and SAMtools. Bioinformatics. 2009;25(16):2078-9.
69. Quinlan AR, Hall IM. BEDTools: a flexible suite of utilities for comparing genomic features. Bioinformatics. 2010;26(6):841-2.
70. Liao Y, Smyth GK, Shi W. featureCounts: an efficient general purpose program for assigning sequence reads to genomic features. Bioinformatics. 2014;30(7):923-30.
71. Smith T, Heger A, Sudbery I. UMI-tools: modeling sequencing errors in Unique Molecular Identifiers to improve quantification accuracy. Genome Res. 2017;27(3):491-9.
72. Li B, Gould J, Yang Y, Sarkizova S, Tabaka M, Ashenberg O, et al. Cumulus provides cloud-based data analysis for large-scale single-cell and single-nucleus RNA-seq. Nat Methods. 2020;17(8):793-8.
73. Waskom M. seaborn: statistical data visualization. Journal of Open Source Software. 2021;6(60).
74. Tirosh I, Izar B, Prakadan SM, Wadsworth MH, 2nd, Treacy D, Trombetta JJ, et al. Dissecting the multicellular ecosystem of metastatic melanoma by single-cell RNA-seq. Science. 2016;352(6282):189-96.

“Mesenchymal Osr1 cells orchestrate lymph node initiation”

Pedro Vallecillo-García[1,10,*], Mickael Orgeur[2], Glenda Comai[3], Sophie Poehle-Kronnawitter[1], Cornelius Fischer[4], Marleen Gloger[5,6], Camille Dumas[7], Claudia Giesecke-Thiel[8], Sascha Sauer[4], Robert Kelly[7], Shahragim Tajbakhsh[3], Uta E. Höpken[9] and Sigmar Stricker[1,*]

Supplementary figure 1

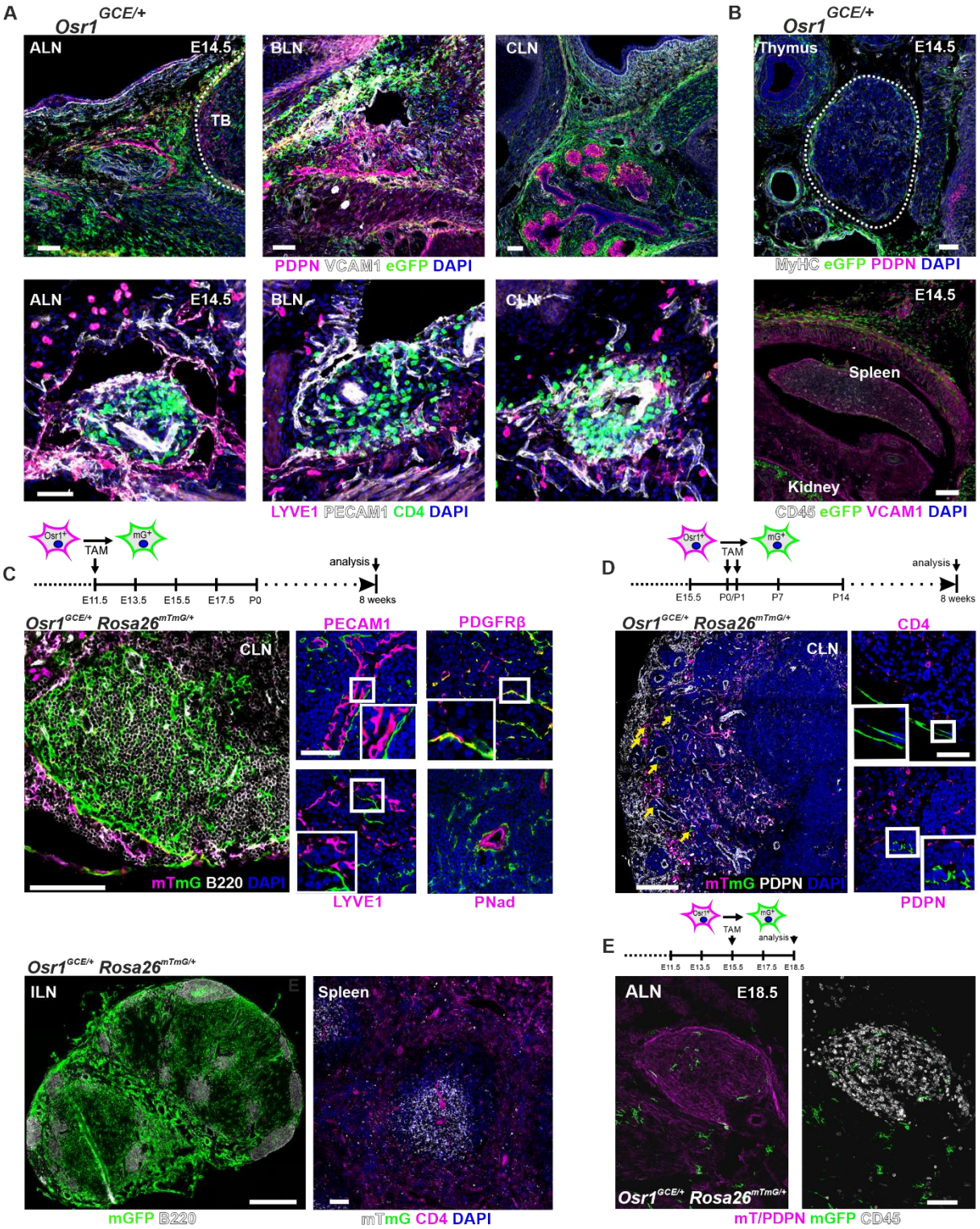

S1 related to figure 1. *Osr1 embryonic expression and lineage contribution to primary and secondary lymphoid organs*. ***(A)*** *Immunofluorescence of E14.5 Osr1$^{GCE/+}$ peripheral LN regions identifying LN anlagen. Antibodies against PDPN, LYVE1, PECAM1, VCAM1, CD4 and eGFP (Osr1) were used to label lymphatic vasculature, blood vasculature, mesenchymal LTos and LTis.* ***(B)*** *Osr1 is not expressed in E14.5 Osr1$^{GCE/+}$ thymus and spleen; co-staining for MyHC, Osr1, PDPN in thymus and CD45, Osr1 and VCAM1 in the spleen. Dashed line demarcates the thymus.* ***(C)*** *Schematic representation of Cre recombinase induction at the stage E11.5. Lineage contribution was assessed at 8 weeks of age. Immunofluorescence of CLN sections for membrane GFP and B220 demarcates B cell follicle. Embryonic E11.5 Osr1 cells contribute to vasculature associated fibroblasts, in the proximity of blood vessels (PECAM1), lymphatic vessels (LYVE1), high endothelial venules (PNad) and mural cells (PDGFRβ). Higher magnification of the boxed regions is shown at the bottom corner. Below, E11.5/E12.5 Osr1 descendants contribute to inguinal LN but are not found in the splenic stroma.* ***(D)*** *Contribution of Osr1 cells to adult*

mesenchymal stromal cells decreases at late stages of development. Schematic representation of perinatal (P0 and P1) tamoxifen induction. mGFP cells are sparsely found in the CLN. Higher magnification of the boxed regions is shown at the bottom. ***(E)*** *Low E15.5 Osr1 contribution is shown in the axillary LN of E18.5 embryos. Sparse mGFP+ cells are found in the LN anlage and surrounding tissues. Representative immunofluorescence images were captured from at least 3 independent experiments. Scale bar represents in* ***(A)*** *200 µm,* ***(B)*** *50 µm (thymus) and 100 µm (spleen),* ***(C, D)*** *100 µm and* ***(E)*** *200 µm. CLN represents cervical LN.*

Supplementary figure 2

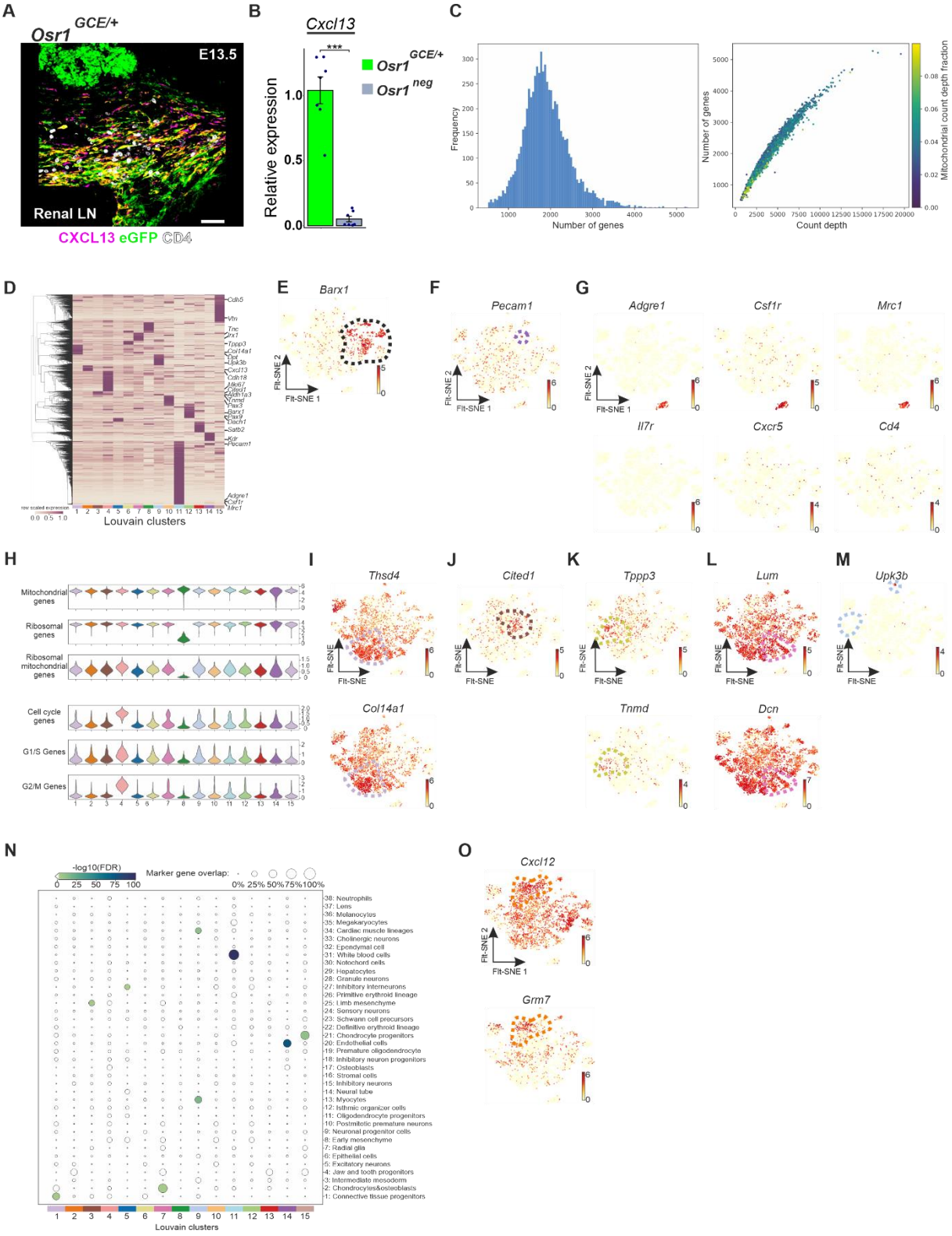

S2 related to figure 2. *E13.5 Osr1 scRNA-seq unravels Osr1+ cell heterogeneity.* ***(A)*** *3D reconstruction of E13.5 Osr1^{GCE} renal LN. Immunofluorescence of 35 µm cross-sections shows CXCL13 and Osr1 co-expression in close association with CD4 LTi cells. Immunofluorescence is representative image of at least 3 independent experiments. Scale bar represents 50 µm.* ***(B)*** *Cxcl13 expression is restricted to Osr1$^{GCE/+}$ cells. Relative Cxcl13 expression from FACS sorted E13.5 Osr1 positive (Osr1$^{GCE/+}$) and Osr1 negative cells.* ***(C)*** *Quality plots showing the number of genes (left) and counts (right) detected per cell in single cell sequencing of Osr1+ E13.5 cells.* ***(D)*** *Hierarchical clustering of 7730 upregulated genes detected across all Louvain clusters with a percentage fold change of at least 2 between the percentage of expressing cells in a given cluster relative to all other clusters. Gene expression level was averaged across all cells for each cluster. Key genes used to define the 15 clusters are indicated on*

the right. ***(E-G)*** *FIt-SNE visualization of cells expressing the indicated genes.* ***(H)*** *Violin plots depicting the distribution of averaged gene expression in all cells per Louvain cluster for mitochondrial, ribosomal and cell cycle genes.* ***(I-M)*** *FIt-SNE visualization of cells expressing the indicated genes.* ***(N)*** *Cell type enrichment analysis of Louvain clusters with embryonic cell populations defined from E9.5-E13.5 mouse embryos based on marker gene overlap. Overlaps with a false discovery rate (FDR) below 0.01 were considered as significant.* ***(O)*** *FIt-SNE visualization of cells expressing the indicated genes. In* ***(E-G, I-M, O),*** *gene expression level in cells is depicted as log-transformed normalized counts. Cells for the scRNA-seq analysis were derived from a single E13.5 Osr1$^{GCE/+}$ embryo.*

Supplementary figure 3

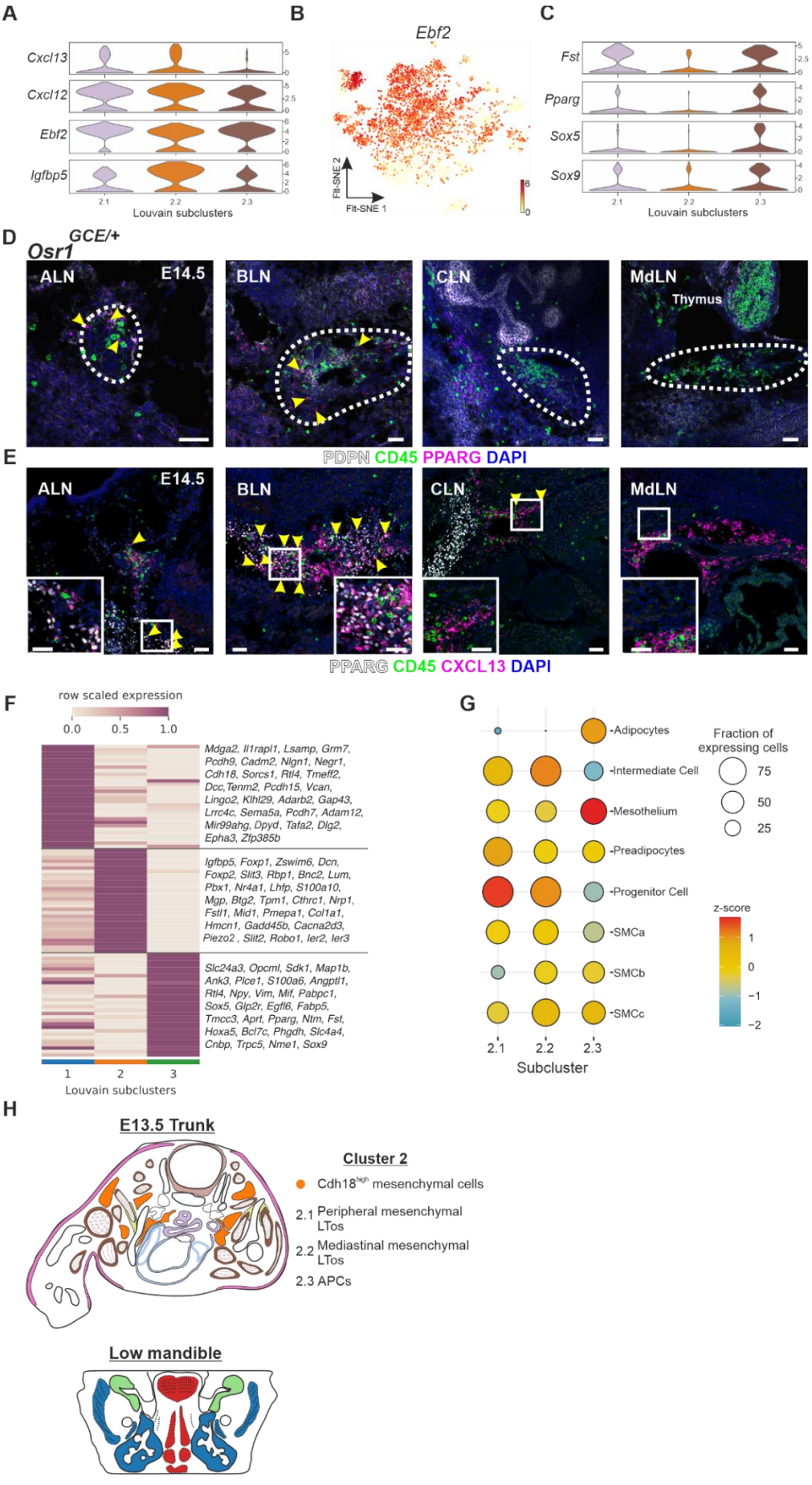

S3 related to figure 3. *APCs and mesenchymal LTos are derived from a common Osr1 embryonic progenitor in the trunk.* ***(A)*** *Violin plots of selected genes depicting the distribution of gene expression within all cells per Louvain subcluster of cluster 2.* ***(B)*** *FIt-SNE visualization of cells expressing Ebf2 in all Osr1 cells. Color bars represent the gene expression level in cells as log-transformed normalized counts.* ***(C)*** *Violin plots of selected genes depicting the distribution of gene expression within all cells per Louvain subcluster of cluster 2.* ***(D)*** *PPARG positive cells are found in close association to LNs. Representative micrographs of E14.5 Osr1$^{GCE/+}$ peripheral and mediastinal LN anlage. CD45 are confined to the LN anlage (dashed line) in close proximity to PPARG positive APCs* ***(E)*** *Immunofluorescence of E14.5 LNs for CXCL13 and PPARG shows partial co-expression in ALN and BLN. Yellow arrows are pointing to PPARG nuclei surrounded by CXCL13 expression in BLN, ALN and CLN. Higher magnification of the boxed region is shown as inserts.* ***(F)*** *Clustering of 30 most upregulated genes in each Louvain subcluster. Genes used to define the 3 subclusters are indicated on the right.* ***(G)*** *Dot plot depiction of cell type enrichment analysis for Louvain subclusters 2.1, 2.2 and 2.3. Enrichment analysis was performed using transcriptional signatures of E18.5/P3 aortic stromal vascular fraction and the 35 most upregulated genes in each Louvain subcluster. Expression levels of all upregulated genes were averaged across all cells for each cell subpopulation.* ***(H)*** *Schematic representation of putative cluster identity including cluster 2 subpopulations in the trunk and mediastinal cavity. Immunofluorescence are representative images of at least 3 independent experiments. Scale bar represents in* ***(D, E)*** *50 µm.*

Supplementary figure 4

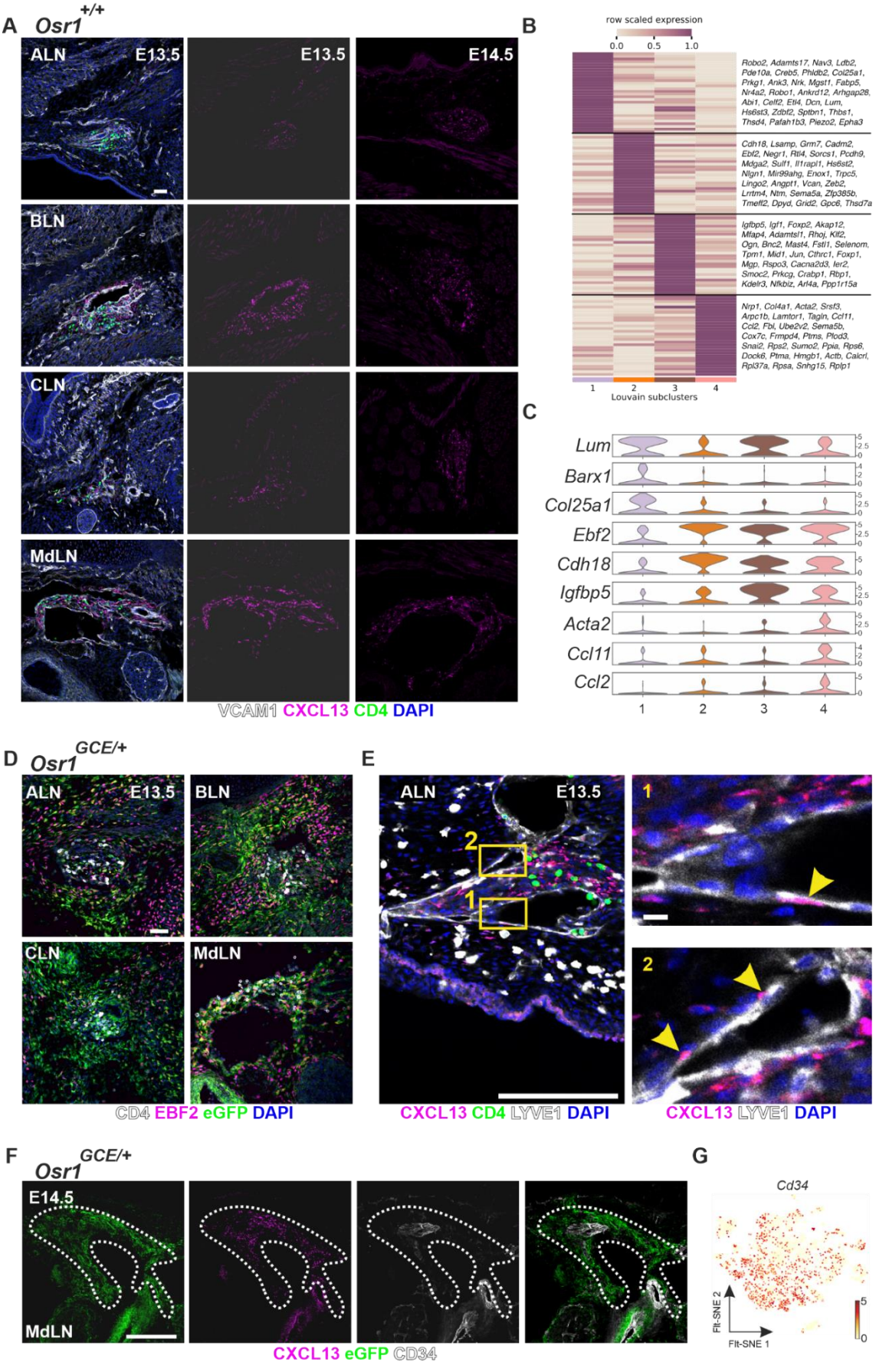

***S4 related to figure 4**. A heterogenous cell population contributes to LTi attraction in the LN anlage **(A)** Heterogenous CXCL13 expression on E13.5 and E14.5 ALN, BLN, CLN and mediastinal LNs. CD4 (green) labels LTis, CXCL13 labels mesenchymal LTos and VCAM1 is highly expressed in blood vessels. **(B)** Clustering of 30 most upregulated genes in each Louvain subcluster. Genes used to define the 4 subclusters are indicated on the right. **(C)** Violin plots of selected genes depicting the distribution of gene expression within all Cxcl13+ cells per subcluster. **(D)** Immunofluorescence of E13.5 ALN, BLN, CLN and mediastinal LN showing EBF2 and Osr1 co-expression in ALN, BLN and mediastinal LN. In the CLN, mesenchymal LTos express low amount of EBF2. **(E)** In the axillary LN anlage of E13.5 embryos, CXCL13 is found in some LYVE1 positive LECs. LTis are labeled in green for CD4. Higher magnification of the boxed regions is shown on the right. Arrows are pointing to cells co-expressing CXCL13 and LYVE1. **(F)** CD34 is expressed at low level by E14.5 mesenchymal LTos in the mediastinal LN anlage. Low CD34 expression is found in few Osr1+ cells in the CXCL13+ area (dashed lines). **(G)** FIt-SNE visualization of cells expressing Cd34 in all Osr1 cells. Color bars represent the gene expression level in cells as log-transformed normalized counts. Immunofluorescence are representative images of at least 3 independent experiments. Scale bar represents in **(A, C)** 50 µm and in **(D)** 200 µm and 20 µm (magnification).*

Supplementary figure 5

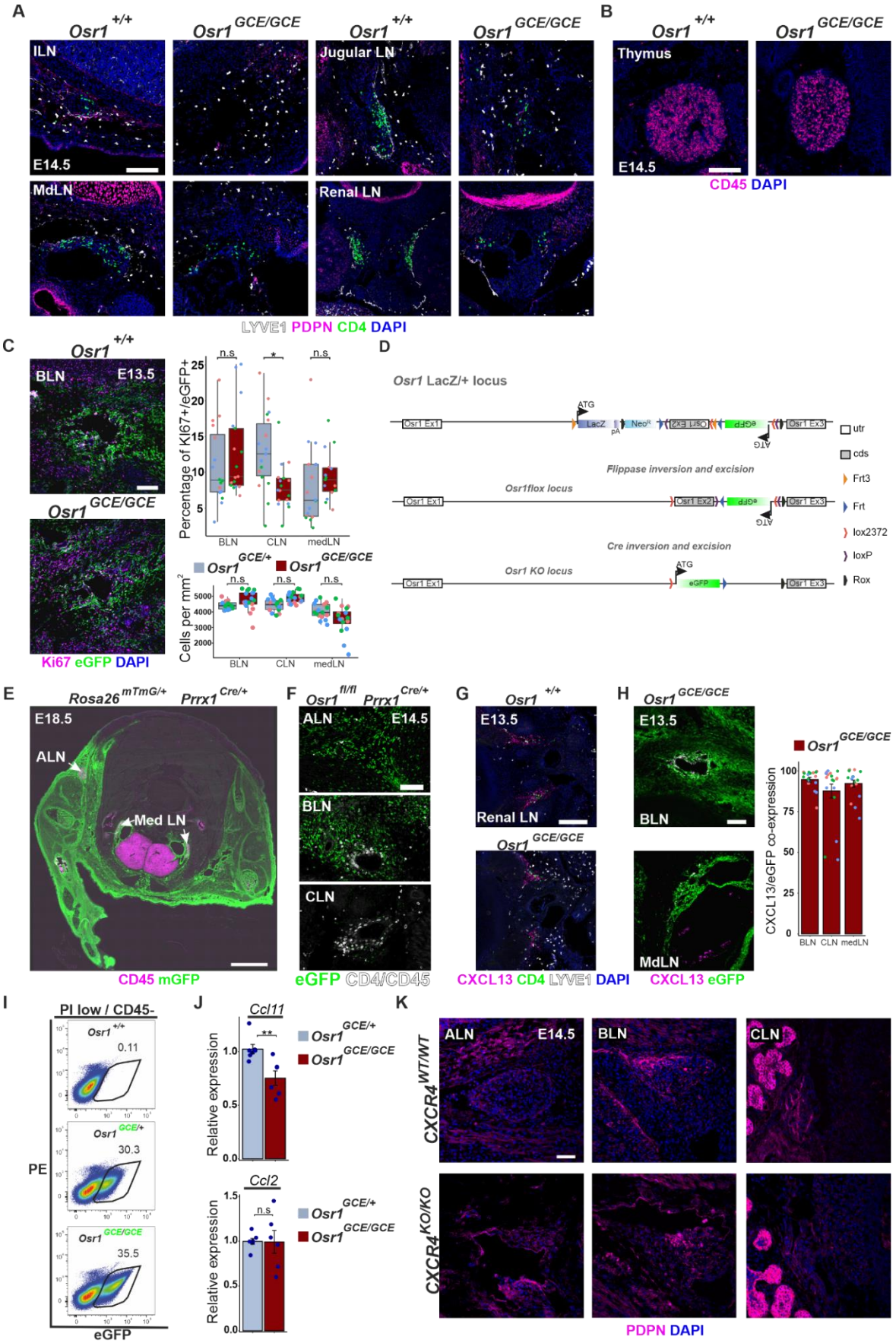

S5 related to figure 5*. Osr1 controls mesenchymal LTo commitment and formation of accessorial lymphatic vasculature.* ***(A)*** *Representative immunofluorescence of inguinal, mediastinal, jugular and renal LN anlagen in E14.5 Osr1$^{+/+}$ and Osr1$^{GCE/GCE}$*

embryos using anti CD4 and PDPN antibodies showing impaired LN initiation. ***(B)*** *Thymus morphology assessed by CD45 immunofluorescence is normal in E14.5 $Osr1^{GCE/GCE}$ embryos as compared to $Osr1^{+/+}$ littermates.* ***(C)*** *Cell proliferation and cellularity were assessed in E13.5 $Osr1^{GCE/+}$ and $Osr1^{GCE/GCE}$ embryos. Left, representative images of immunofluorescences using anti KI67 and anti GFP antibodies. Right, quantification of Ki67+ eGFP+ cells at the designated LN anlage and nuclei per area in E13.5 $Osr1^{GCE/+}$ and $Osr1^{GCE/GCE}$ sections (n=3).* ***(D)*** *Schematic representation of $Osr1^{LacZ}$ locus transformation into an $Osr1^{fl}$ locus showing flippase and Cre recombinase events and reorganization of the eGFP cassette.* ***(E, F)*** *Recombination of the $Osr1^{fl}$ locus via Prrx1-Cre driven expression assessed via immunofluorescence in E14.5 ALN, BLN and CLN of $Osr1^{fl/fl}$ $Prrx1^{Cre}$ embryos. An anti GFP antibody was used to label recombined Osr1+ cells and CD45/CD4 for LTis.* ***(G)*** *CXCL13 reduction in E13.5 $Osr1^{GCE/GCE}$ embryos at the renal LN anlage. CD4 labels LTis and LYVE1 LECs.* ***(H)*** *Representative images of E13.5 $Osr1^{GCE/GCE}$ LN anlage labeled for CXCL13 and Osr1. In E13.5 $Osr1^{GCE/GCE}$ embryos, residual CXCL13 expression is restricted to mesenchymal Osr1-eGFP+ cells. Right, quantification of CXCL13 signal expressed by Osr1+ cells (n=3).* ***(I)*** *FACS strategy for mesenchymal Osr1+ cell isolation from E13.5 $Osr1^{GCE/+}$ and E13.5 $Osr1^{GCE/GCE}$ embryos (n=5).* ***(J)*** *Ccl11 expression was reduced and Ccl2 remained unchanged in E13.5 $Osr1^{GCE/GCE}$ homozygous FACS sorted cells when compared to $Osr1^{GCE/+}$ heterozygous cells, n=6.* ***(K)*** *Lymphatic vasculature labeled with PDPN is not significantly impaired in LN anlage of E14.5 $CXCR4^{KO/KO}$ embryos. Immunofluorescence are representative images of at least 3 independent experiments. Scale bar represents in* ***(A, B, C, F, G, H, K)*** *100 µm and in* ***(E)*** *1 mm. Error bar represents SEM. P-values were obtained from student's t-test, ** $p<0.01$ or n.s not significant.*

Supplementary figure 6

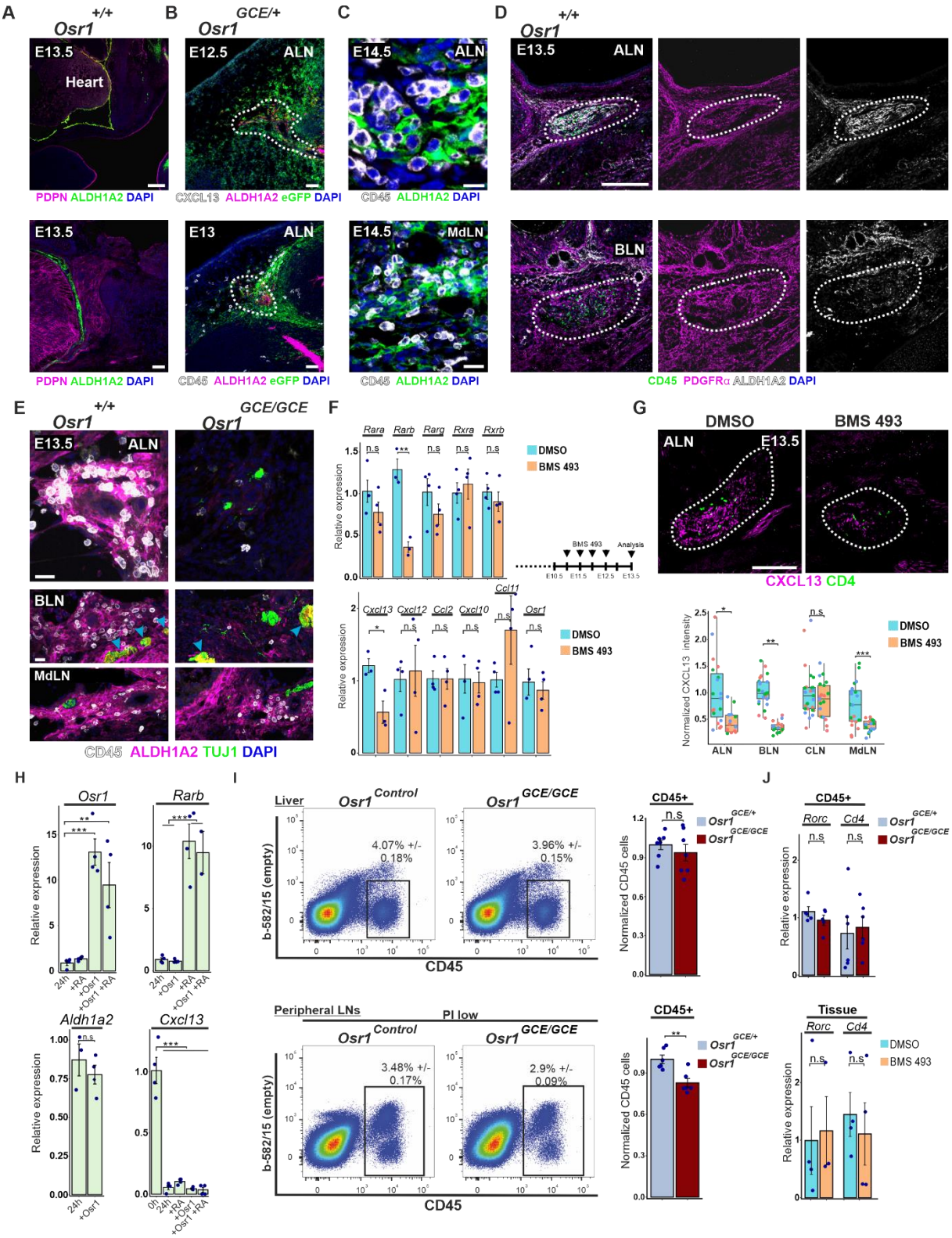

S6 related to figure 6. *Mesenchymal RA promotes mesenchymal LTo commitment.* ***(A)*** *High expression of ALDH1A2 in epicardial and meningeal fibroblast of E13.5 control embryos. Immunofluorescence of E13.5 tissues using antibodies against ALDH1A2 and PDPN confirmed specific ALDH1A2 staining.* ***(B)*** *In E12.5 and E13 Osr1$^{GCE/+}$ axillary region Osr1 and ALDH1A2 are expressed in mesenchymal cells surrounding the junction of the thoracic artery. Mesenchymal LTos were labelled by CXCL13, immune cells by CD45. Dashed lines demarcate presumptive ALN.* ***(C)*** *High magnification micrographs of E14.5 ALN and mediastinal LN showing exclusive ALDH1A2 expression in mesenchymal LTos. CD45 labelled LTis.* ***(D*** *Immunofluorescence of E13.5 tissues using antibodies against CD45, PDGFRα and ALDH1A2. Note high correlation of PDGFRα and ALDH1A2 signals in E13.5 axillary and brachial LN anlage.* ***(E)*** *High magnification depiction of ALN, BLN and mediastinal LN that highlights*

ALDH1A2 reduction in mesenchymal LTos of E13.5 Osr1$^{GCE/GCE}$ embryos. Motoneurons stained with TUJ1 do not present reduced ALDH1A2 expression. CD45 was used to label LTis. ***(F)*** *RA inverse agonist BMS493 treatment only affects Rarβ expression. Relative measurement of gene expression of RAR genes in E13.5 control (DMSO) and BMS493 treated embryos (n=3-4). Below, only the expression of Cxcl13 is compromised in BMS493 treated embryos. Relative expression assessed by RT-qPCR from whole embryonic tissue (n=3-4). Schematic representation of BMS493 administration is shown on the right.* ***(G)*** *Representative immunofluorescence of E13.5 BLN treated with the RA inverse agonist BMS493 or DMSO. CXCL13 expression is reduced in ALN, BLN and mediastinal LN as quantified below. Normalized CXCL13 intensity in the LN anlage quantified on sections (n=3).* ***(H)*** *Osr1-FLAG lentiviral infection did not activate Aldh1a2 expression. All-trans retinoic acid (100 nM) activation alone or in conjunction with Osr1-FLAG lentiviral infection did not rescue Cxcl13 downregulation in E13.5 embryonic bodies, whereas Osr1/Rarβ are robustly induced (n=2-4).* ***(I)*** *FACS analysis of CD45+ cells from liver and peripheral tissues of E13.5 Osr1^{Control} (+/+ and GCE/+) and E13.5 Osr1$^{GCE/GCE}$ embryos. A reduction of CD45+ cells was only observed in peripheral tissues (n=6-7).* ***(J)*** *Relative expression of Rorc and Cd4 transcripts measured via RT-qPCR in CD45+ cells from E13.5 Osr1$^{GCE/+}$ or Osr1$^{GCE/GCE}$ embryos and E13.5 tissues of control (DMSO) and BMS493 treated embryos (n=3-4). Rorc and Cd4 expression remains unchanged in all conditions. Immunofluorescence images are representative images of at least 3 independent experiments. Scale bar represents in* ***(A, D, G)*** *200 µm and* ***(A)*** *50 µm (below),* ***(B)*** *50 µm,* ***(C)*** *10 µm and 25 µm (below) and* ***(E)*** *20 µm. In* ***(F, G, H, I and J)****, error bar represents SEM, * p< 0.05, ** p< 0.01, *** p< 0.001 or n.s not significant. In* ***(H),*** *P-values were obtained from one-way ANOVA with Dunnett´s post-hoc comparison and in* ***(F, G, I and J)****, P-values were obtained from student's t-test.*

Supplementary figure 7

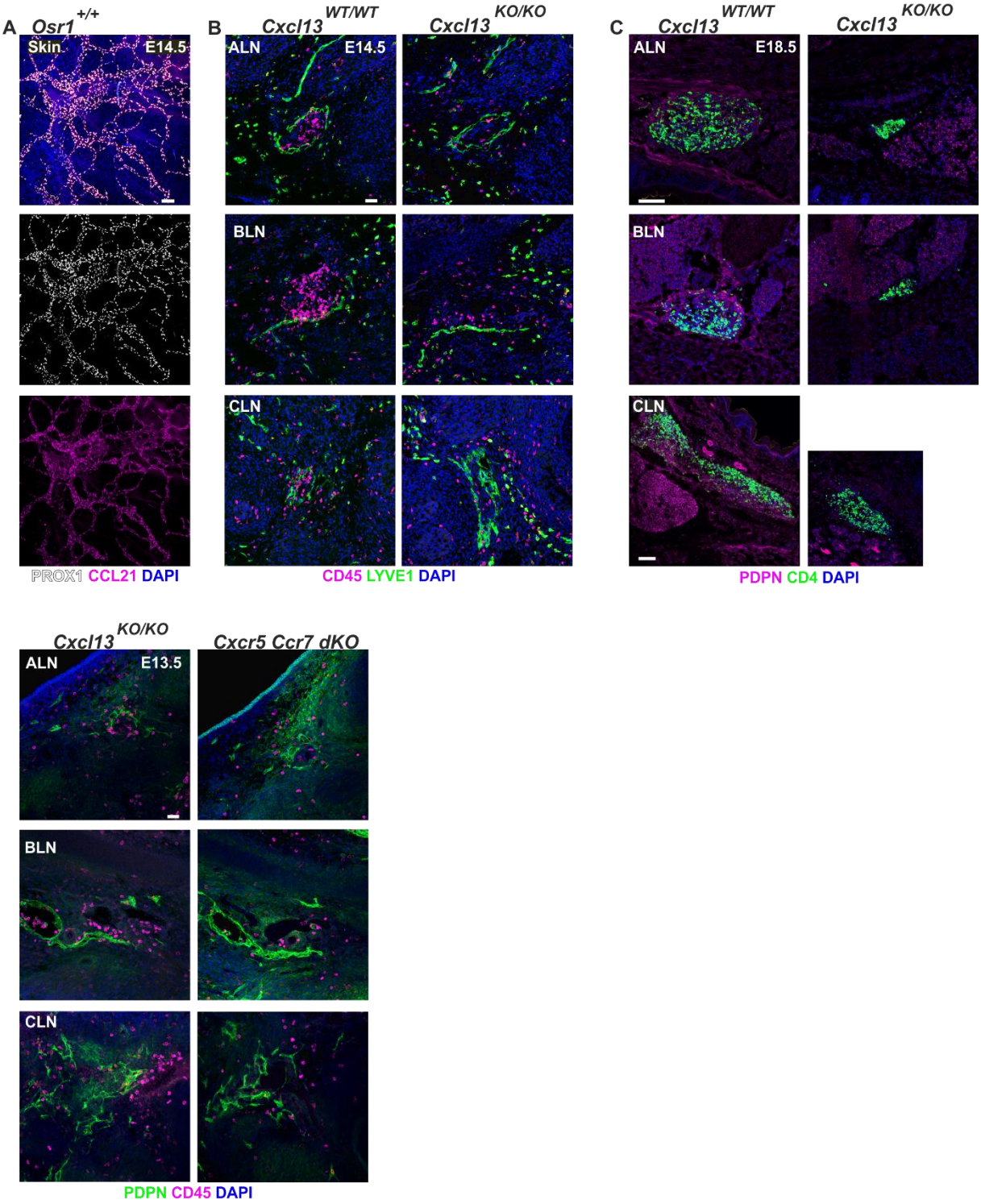

S7 related to figure 7. *Combined action of mesenchymal LTos and LECs is required for LTi attraction in LNs.* ***(A)*** *Skin whole-mount immunofluorescence depicting lymphatic vasculature labeled by PROX1 and CCL21.* ***(B)*** *At the stage E14.5, ALN and BLN anlagen show dissolved LTi-accumulation in CXCL13$^{KO/KO}$ embryos. CD45 labels immune cells and LYVE1 LECs.* ***(C)*** *In E18.5 CXCL13$^{KO/KO}$ embryos, LN impairments are maintained during development. ALN and BLN are not formed and CLN presents a reduced size. Antibodies against CD4 and PDPN were used to label LTis and LECs.* ***(D)*** *Combined CXCR5 and CCR7 deficiency leads to an arrest in LTi accumulation in all PLNs at the stage E13.5. Antibodies against PDPN and CD45 were used to stain lymphatic vasculature and immune cells. Immunofluorescence are representative images of at least 3 independent experiments. Scale bar represents in* ***(A, C)*** *100 µm and* ***(B, D)*** *50 µm.*

Supplementary table 1

Primary antibodies:

Antibody	Clone	Conjugate	Concentration/ Dilution	Source
Mouse anti-MyHC	Monoclonal	Unconjugated	1:500	Chemicon
Chicken anti-GFP	Polyclonal	Unconjugated	1:1000	Aves
Rabbit anti-α-SMA	Polyclonal	Unconjugated	2 µg ml^{-1}	Abcam
Hamster anti-Pecam1	Polyclonal	Unconjugated	1:250	DSHB (2H8)
Rabbit anti-Col12a1	Polyclonal	Unconjugated	1:500	M. Koch
Goat anti-collagen I	Polyclonal	Unconjugated	1:400	Novus Biologicals
Hamster anti PDPN	Polyclonal	Unconjugated	1:100	DSHB (8.1.1)
Rat anti CD4	GK 1.5	Unconjugated	1:100	Biolegend
Rat anti B220	RA3-6B2	Alexa Fluor ® 594	1:100	Biolegend
Rat anti CD21/35	7E9	Alexa Fluor ® 594	1:100	Biolegend
Rat anti MadCAM1	MECA-367	Unconjugated	1:100	Biolegend
Rat anti PNad	MECA-79	Unconjugated	1:100	Biolegend
Rat anti CD45	30-F11	Unconjugated	1:100	Biolegend
Rat anti ERTR7	ER-TR7	Unconjugated	1:100	BioRad (MCA2402)
Rabbit anti TNC	Polyclonal	Unconjugated	1:200	Chemicon
Rabbit anti LUM	Monoclonal	Unconjugated	1:50	CUSABIO
Goat anti IGFBP5	Polyclonal	Unconjugated	1:200	R&D System (AF578)
Sheep anti EBF2	Polyclonal	Unconjugated	1:20	R&D System (AF7006)
Rabbit anti PPARG	81B8	Unconjugated	1:150	Cell Signaling (81B8)
Goat anti CXCL13	Polyclonal	Unconjugated	10 µg ml^{-1}	R&D System (AF470)
Rabbit anti PROX1	Polyclonal	Unconjugated	1:200	ReliaTech
Rabbit anti LYVE1	Polyclonal	Unconjugated	1:200	Abcam (33682)
Mouse anti VCAM1	Polyclonal	Unconjugated	1:100	DSHB (P3C4)
Goat anti CCL21	Polyclonal	Unconjugated	10 µg ml^{-1}	R&D System (AF457)
Rabbit ALDH1A2	Polyclonal	Unconjugated	1:100	Abcam (75674)
Rat anti PDGFRβ	APB5	PE	1:100	Biolegend
Mouse anti TUJ1	TUJ1	Unconjugated	1:200	Biolegend
Goat anti PDGFRα	Polyclonal	Unconjugated	1:100	Cell Signaling
Mouse anti CD34	RAM34	Unconjugated	1:100	BD PharMingen
Rabbit anti-Ki67	Polyclonal	Unconjugated	1:100	Abcam

Supplementary table 2

FACS antibodies

Antibody	Clone	Conjugate	Concentration/ Dilution	Source
Rat anti-T119	TER-119	APC	1:100	eBioscience
Rat anti CD31	390	APC	1:100	eBioscience
Rat anti IL-7R	A7R34	Alexa Fluor 488	1:100	Biolegend
Rat anti CD4	GK 1.5	APC-Cy7	1:100	Biolegend
Rat anti CD3	17A2	PE	1:100	Biolegend
Hamster anti CD11c	N418	PE	1:100	Biolegend
Rat anti PDPN		Alexa Fluor 594	1:100	Biolegend
Rat anti-CD45	30-F11	APC	1:100	eBioscience
Anti-Sca1	D7	APC-Cy7	1:100	eBioscience
Anti-PDPN	8.1.1	APC-Cy7	1:100	Biolegend

Supplementary table 3

Secondary antibodies:

Antibody	Conjugate(s)	Source
Donkey anti-mouse	Alexa Fluor 488, 568 and 680	Molecular Probes
Donkey anti-rabbit	Alexa Fluor 488, 568 and 647	Molecular Probes
Donkey anti-goat	Alexa Fluor 488, 568 and 680	Molecular Probes
Goat anti-hamster	Alexa Fluor 488, 568	Molecular Probes
Donkey anti-rat	Alexa Fluor 488, 568, 647	Molecular Probes
Donkey anti-chicken	Alexa Fluor 488	Molecular Probes
Donkey anti-sheep	Alexa Fluor 488, 568	Molecular Probes

Supplementary table 4

Primer sequences (RT-qPCR):

Gene	Forward	Reverse
Gadph	CTGCACCACCAACTGCTTAG	GGATGCAGGGATGATGTTCT
Cxcl13	CAACGCTGCTTCTCCTCCT	CAGGGGGCGTAACTTGAAT
Cxcl12	GCTCCACCCACAAGGTTAAG	CTGGCAGAAGGCCTTGAATA
Cxcl10	CATCCTGCTGGGTCTGAGTG	TGATCTCAACACGTGGGCAG
Ccl2	AGGTCCCTGTCATGCTTCTG	GCTGCTGGTGATCCTCTTGT
Ccl11	TCCATCCCAACTTCCTGCTG	TGGGGTCAGCACAGATCTCT
Osr1	GCACACTGATGAGCGACCT	TGTAGCGTCTTGTGGACAGC
Aldh1a2	GGATGCGTCTGAAAGAGGAC	CCCAGCCTGCATAATACCTC
Cyp26b1	GCTCATCGGAGAGACTGGTC	CCAGTAGGATCTTGCGCACA
Rarb	CTTCAAAGCAGGAATGCACA	GGCCAGCTCACTGAATTTGT
Rara	AAATCATCCGGCTACCACT	TCTGGATGCTTCGTCGGAA
Rxra	TCAGTACTGCCGCTACCAGA	GTCTCAGTCTTGGGCTCGAC
Rxrb	CTGCAAGGGTTTCTTCAAGC	ATCTCCATCCCCGTCTTTGT
Rorc	CAGAATGTGCAGGGCCTACA	GAAAAACACAGGGCGCTGAG
Cd4	TTCACCTGGAAGTTCTCTGACC	AACGATCCTTTCTCCCATGC
Il7ra	GGACGATCACTCCTTCTGGT	TTGCAGCTTGTTAAGAGTTAGGC
Osr1	GCACACTGATGAGCGACCT	TGTAGCGTCTTGTGGACAGC
Cl-Cxcl13	TTCAAGTCTTTGCCGAAGGT	TGAGACTCTTTGTTGCTGTTGG
P-Cxcl13	GATGGTTGTGTGTATGACAAGGA	GAGGGTGTGTCTCCATTGCT
Cr-Cxcl13	GTGCAGGCAGGTGTAGAGC	GAATAGGTGTGGCCTTGCTG
Cl-Aldh1a2	CATGGGGATAGAGGCAGAAA	AGAATCTCCGGGTTGAGCTT
P-Aldh1a2	GAGGAAGGCAGATGGGAAAT	CTTGGAAGGTAAGGGAGTGTG